

SEA WAVES MODELING WITH X-BAND COSMO-SKYMED® SAR DERIVED WIND FIELD FORCING AND APPLICATIONS IN COASTAL VULNERABILITY ASSESSMENT

G. Benassai¹, A. Montuori², M. Migliaccio² and F. Nunziata²

[1]{Dipartimento di Scienze Applicate, Università di Napoli Parthenope, Napoli, Italy}

[2]{Dipartimento per le Tecnologie, Università di Napoli Parthenope, Napoli, Italy}

Correspondence to: A. Montuori antonio.montuori@uniparthenope.it

Abstract

In this paper, X-band COSMO-SkyMed® synthetic aperture radar (SAR) wind field data are first experimented as forcing of coastal wind-wave modeling for both sea-wave numerical simulation and coastal vulnerability assessment purposes. The SAR-based wind field retrieval is accomplished by resolving the SAR-based wind speed and the wind direction retrieval problems independently. The sea surface wind speed is retrieved through the azimuth cut-off procedure and the sea surface wind direction is determined by the multi-resolution analysis of the discrete wavelet transform. The wind-wave modeling is based on the third-generation Simulating WAVes Nearshore (SWAN) model, which is used for sea wave state estimation in coastal and inland regions. The coastal vulnerability assessment is provided by means of a key parameter, known as impact index, which consistently evaluates the coastal risk due to the inundation of the inshore land. Experiments consist of SWAN numerical simulations run with respect to some relevant wave storms recorded in the southern Tyrrhenian Sea on 2010, with applications in coastal vulnerability assessment along the coastal plain of river Sele. Experimental results show the benefits of blended wind field products, provided by European Centre for Medium Weather Forecast (ECMWF) model winds and SAR-based wind field estimations, for both wind-wave modeling and coastal vulnerability assessment purposes.

1 **1 Introduction**

2 The physical, chemical and biological interactions between the ocean and the atmosphere are
3 of great applicative relevance since they affect climate variability and Earth system dynamics
4 (Janssen, 2004; Harlan, 2005). In fact, the oceans and the atmosphere have the capability to
5 store and exchange energy in the form of heat, moisture, and momentum, whose changes
6 affect the climate engine of the whole planet on a large space-temporal scale (Janssen, 2004;
7 Harlan, 2005). The monitoring and the forecasting of wind-wave interaction processes
8 become particularly critical along the coastal areas, which are highly dynamic and
9 geomorphologically complex systems that respond in a non-linear manner both to extreme
10 weather conditions and, more generally, to external perturbations (Benassai, 2006; Di Paola,
11 2011; Alberico et al., 2012). Moreover, the impact of climate change along the coastal regions
12 may include the presence of events that severely affect the Earth system dynamics, such as the
13 possible increase of sea surface temperatures as well as the changes in frequency, intensity
14 and duration of wave storms (Benassai, 2006; Di Paola, 2011; Alberico et al., 2012).

15 Based on this rationale, the evolution of winds, waves and the wind-driven sea circulation is
16 of great applicative relevance not only for the modeling and the forecasting of both weather
17 and climate, but even for the observation of oceanographic phenomena (e.g. floods, storms
18 and tides activities) and coastal vulnerability assessment processes.

19 In the following, the state of the art relevant to the wind-wave modeling and the coastal
20 vulnerability assessment procedure is briefly described.

21 With respect to the wind-wave modeling, advanced spectral models known as third-
22 generation models have been developed and validated in the last decades to solve the spectral
23 action balance equation without any a priori spectrum restrictions for the evolution of the
24 wave growth (WAMDI Group, 1988; Tolman, 1991; Booij et al., 1999; Benassai and Ascione,
25 2006). They are able to describe the physical processes of wave generation, dissipation and
26 wave-wave interaction, overcoming the constraints of first- and second-generation wind-wave
27 models (WAMDI Group, 1988; Tolman, 1991; Booij et al., 1999; Benassai and Ascione,
28 2006). Moreover, third-generation models predict directional spectra and wave properties,
29 such as significant wave height, mean wave direction and frequency, swell wave height and
30 mean direction, and wind stress fields.

31 The first prototypical third-generation wave model is the WAM, where the two-dimensional
32 wave spectrum is allowed to freely evolve without constraints on the spectral shape (WAMDI

Group, 1988). Similarly, the second third-generation wind-wave model, known as WAVEWATCH III (Tolman, 1997, 1999, 2009) employs a third-order numerical propagation scheme to control numerical diffusion of swell. Nowadays, the most used third-generation wind-wave modeling is the Simulating WAVes Nearshore (SWAN) model, which computes random, short-crested wind-generated waves in coastal regions and inland waters (Booij et al., 1999; Benassai, 2006; Benassai and Ascione, 2006). It is based on the Eulerian formulation of the discrete spectral action density balance equation, which accounts for refractive propagation over bathymetry and current fields. Driven by boundary conditions and local wind fields, the SWAN model allows describing the processes of wind generation, white capping, quadruplet wave-wave interactions and bottom dissipation (Booij et al., 1999; Benassai, 2006; Benassai and Ascione, 2006).

All the wind-wave models described above require the current state of the sea as initial information (WAMDI Group, 1988; Tolman, 1991; Booij et al., 1999; Benassai and Ascione, 2006). The analysis of sea-state conditions can be created through data assimilation, where buoy or satellite altimeter measurements are combined with a background guess from a previous forecast or climatology to create the best estimate of the current conditions. It is well known that results from wind-wave simulations critically depend on the quality of the driving wind fields, whose uncertainties severely impact the estimated wave properties (Teixeira et al., 1995; Holthuijsen et al., 1996). In addition to the classical forcing provided by forecasting and/or climatological winds, other sources of wind field information have been considered in literature to force wind-wave models, such as the active satellite-based microwave synthetic aperture radar (SAR) (Johannessen et al. 2000; Portabella, 2002; Monaldo et al., 2005). The latter is considered a key alternative source of wind field information able to integrate classical wind field estimation techniques (e.g. meteorological models, in situ observations and scatterometers) due to its high spatial and temporal resolution as well as its ground coverage and short revisit-time (Migliaccio and Repucci, 2006; Yang et al., 2011). Within such a framework, the possibility to retrieve the sea surface wind field from SAR data and then exploit the suitability of this information as forcing of coastal wind-wave modeling is very interesting from an operational viewpoint.

With respect to the coastal vulnerability assessment (CVA), different procedures are proposed in literature that can be distinguished in semi-quantitative and quantitative approaches (Benassai, 2006). The first ones are mainly based on the subjective assessment of

geomorphologic indicators, while the second ones quantify the relative importance of physical and geomorphologic relevant phenomenon. The proposed methodologies have been progressively evolved from single approaches, such as Bruun rule (Bruun, 1962) and UNEP Methodology (Carter et al., 1994), to more recent consistent techniques, such as USGS-CVI (Gornitz et al., 1994) and SURVAS (Nicholls and de la Vega-Leinert, 2000; Benassai et al., 2009). The latter provide improved consideration of both physical and non-physical factors, with the associated uncertainties.

One of the most CVA methods is based on the Coastal Vulnerability Index (CVI) (Gornitz et al., 1994, 1997), which combines the changing susceptibility of the coastal system with its natural capability to adapt to changing environment. The vulnerability classification is based upon the relative contributions and interactions of six variables, i.e. mean elevation, geology, coastal landform, shoreline, wave height and tidal range (Diez et al., 2007).

A different approach has been recently suggested in (Benassai et al., 2009), which evaluates the coastal risk due to the inundation of the inshore land. This method allows assessing the coastal vulnerability by means of a new parameter, known as impact index, which is based on wave, climate, bathymetry and sediment data. It depends on run-up height, seasonal and long-term erosion index, and efficiency of coastal protection structures (Benassai et al., 2009).

In this paper, both sea wave simulations and the CVA are investigated in a coastal environment by first using X-band COSMO-SkyMed© (hereinafter CSK©) SAR-based wind field retrievals as input wind field forcing. The SAR-based wind speed and wind direction retrievals are independently accomplished using the azimuth cut-off procedure and the multi-resolution analysis of the discrete wavelet transform, respectively. SWAN numerical simulations are carried out with respect to some relevant wave storms by using different wind field forcings, i.e. European Centre for Medium Weather Forecast (ECMWF) model winds, SAR-based wind field (i.e. wind speed and direction) retrievals and ECMWF-SAR blended wind fields. The output of wind-wave simulations is then used for CVA purposes to evaluate the impact index of a coastal environment. The suitability of ECMWF-SAR blended wind field product is finally investigated for both wind-wave modeling and CVA purposes.

The paper is organized as follows: the test area and the data set used in this study are given in Section 2. The theoretical background and the methodology at the basis of the X-band SAR wind field retrieval, the wind-wave model and the CVA are given in Section 3. Experimental results are presented and discussed in Section 4. Finally, conclusions are drawn in Section 5.

2 Data set

In this section, the test area and the data set used for SAR-based wind field retrieval, wind-wave numerical simulations and CVA purposes are described.

The test area is the coastal zone of the southern Tyrrhenian Sea, including the Gulfs of Gaeta, Napoli, Salerno and Policastro, which are of great applicative relevance for both oceanographic and coastal-maritime surveillance purposes.

The data set consists of:

- 60 X-band VV-polarized Level 1B DGM ScanSAR Huge Region CSK© SAR data, gathered in the test area during the winter season of 2010 (Italian Space Agency, 2007). They provide ground coverage of about $200\text{km} \times 200\text{km}$ with a spatial resolution of $100\text{m} \times 100\text{m}$. Each SAR data is characterized by large variability for the incidence angle θ ($\sim 10^\circ$) and the whole SAR data set allows covering a broad range of θ values (25° – 60°). Each Level 1B DGM SAR data is characterized by a large number of looks (~ 18) (Italian Space Agency, 2007). The SAR data set is used to retrieve the sea surface wind field (i.e. wind speed and wind direction) information according to the X-band SAR-based wind field estimation methodology described in Section 3.
- Timely and spatially co-located Advanced Scatterometer (ASCAT) wind fields (freely available at <http://podaac.jpl.nasa.gov/>) with a spatial gridding resolution of $12.5\text{km} \times 12.5\text{km}$ in both range and azimuth directions. The ASCAT scatterometer wind field information is used as reference ground truth to evaluate both the effectiveness and the corresponding uncertainties of X-band CSK© SAR-based wind field estimations.
- Timely and spatially co-located ECMWF model wind data (available at: <http://www.ecmwf.int/>), with a spatial gridding resolution of $1/4^\circ$ ($\sim 28\text{km} \times 20\text{km}$ in range and azimuth directions, respectively) and a time resolution of 6h. The ECMWF model winds are used together with X-band CSK© SAR-based wind field estimations to construct a blended wind field product as forcing of both the wind-wave modeling and the CVA approach described in Section 3.
- Timely and spatially co-located wave field data provided by in situ National buoys system observations (available on line at: http://www.idromare.it/analisi_dati.php) off the island of Ponza. The buoys-related wind-wave information is used as reference ground truth for both wind-wave modeling and CVA purposes.

3 Methodology

In this section, the theoretical background and the methodology at the basis of the X-band SAR-based wind field retrieval, the sea wave numerical simulations and the CVA are given.

3.1 X-band SAR wind field retrieval algorithm

The methodology and the physical background of the X-band SAR-based wind field retrieval approach is now presented and specialized for X-band VV-polarized Level 1B DGM ScanSAR Huge Region mode CSK© SAR data.

The proposed approach consists of two subsequent steps; each of them is made of two sub-steps. At the first step, the SAR image quality is improved while at second step the sea surface wind field is retrieved through X-band SAR measurements.

SAR-based wind field estimation is strongly affected by SAR data quality; hence a pre-processing analysis is necessary to improve SAR image quality. In fact, on one side, X-band SAR data may be affected by tropospheric and atmospheric phenomena (e.g. rain cells, cloud coverage, oceanic fronts, convective cells, etc.) that, especially at higher frequencies, can drastically hamper the SAR imagery interpretability and therefore the retrieval of some meaningful geophysical parameters, such the sea surface wind field (Lee et al., 1995). On the other side, the peculiar burst acquisition mode of ScanSAR SAR measurements is characterized by the presence of the scalloping, i.e. periodic processing anomalies appearing as bars in SAR imagery, that strongly affects the accuracy of SAR-based wind field estimation (Schiavulli et al., 2011, 2012).

Hence, an automatic two-sub-steps pre-processing procedure, first developed in (Schiavulli et al., 2011), is used to improve the quality of SAR images. The first sub-step aims at removing the scalloping pattern by means of a DWT-MRA filtering technique (Mallat, 1989; Schiavulli et al., 2011, 2012). This approach naturally describes the directional features of an image at different spatial scales and therefore it is able to firstly highlight and then remove the scalloping pattern. As demonstrated in (Schiavulli et al., 2011, 2012) for this CSK© SAR data product, the end user has no access to the SAR raw data and then only a sub-optimal de-scalloping post-processing procedure can be implemented. It is worth nothing that Italian Space Agency, after the illustration of these results, claimed for a new SAR raw data processing chain to be developed in the future. The second sub-step of the pre-processing

procedure filters out all the atmospheric phenomena by means of a phenomenological homogeneity test based on the variance to mean square ratio (VMSR) of SAR image power spectral density (Schultz-Stellenfleth et al., 2004; Schiavulli et al., 2011). This sub-step is able to univocally discriminate among sea, i.e. homogeneous, and non-homogeneous parts of SAR images, such as ships, coastline and atmospheric fronts.

The second step of the X-band SAR-based wind field retrieval consists in providing independent estimates of sea surface wind speed (sub-step one of step two) and wind direction (sub-step two of step two).

The SAR-based wind speed estimation is accomplished by means of an algorithm based on the azimuth cut-off procedure (Chapron et al., 1995; Kerbaol, 1998; Korsbakken et al., 1998; Migliaccio et al., 2012; Montuori et al., 2012), which allows consistently retrieving the sea surface wind speed without requiring both any a priori wind direction information and the calibration accuracy of SAR normalized radar cross section (NRCS) measurements of the observed scene. The physical rationale at the basis of the azimuth cut-off procedure lies on the well-known azimuthal Doppler mis-registration due to the orbital motion of sea surface waves (Chapron et al., 1995; Kerbaol, 1998; Korsbakken et al., 1998). The latter affects the sea surface SAR imaging and depends on both sensor's parameters (e.g. platform altitude, velocity, etc.) and sea surface geophysical parameters (Chapron et al., 1995; Kerbaol, 1998; Korsbakken et al., 1998). Moreover, it limits the shortest detectable wavelength in the azimuth direction λ_c , which is a key cinematic parameter that, accounting for sea waves orbital motions within SAR integration time, can be considered a robust indicator of the sea surface wind speed (Chapron et al., 1995; Kerbaol, 1998; Korsbakken et al., 1998). Based on this rationale, a SAR wind speed algorithm based on the azimuth cut-off procedure has been developed and tested for C-band SAR measurements only (Chapron et al., 1995; Kerbaol, 1998; Korsbakken et al., 1998). Following this approach, λ_c is retrieved from the noise-free SAR auto-correlation function (ACF) and physically related to the sea surface wind speed using a linear semi-empirical model:

$$U_{10} = a(\lambda_c - \Lambda) \quad , \quad (1)$$

where U_{10} (m/s) is the wind speed at 10m above the sea surface, Λ (m) is the SAR nominal azimuth resolution and a (1/s) is an empirical parameter. The physical rationale of the azimuth cut-off procedure has been recently extended and tested to X-band VV-polarized

Level 1B DGM ScanSAR Huge Region CSK© SAR measurements (Migliaccio et al., 2012; Montuori et al., 2012).

The SAR-based wind direction estimation is accomplished by using the DWT-MRA approach (Du et al., 2002; Horstmann et al., 2002; Schiavulli et al., 2011). The rationale of this technique relies on the fact that some wind-induced pattern texture features on the sea surface are aligned to the local wind field. These features, which are visible on SAR imagery, are interpreted as manifestations of either atmospheric boundary layer (ABL) rolls, which account for interactions between the atmosphere and the sea surface, or other marine features, such as streaks from foam or more-generally marine surfactants (Du et al., 2002; Horstmann et al., 2002; Schiavulli et al., 2011). These phenomena appear in SAR imagery as adjacent periodic bands of bright and dark radar returns thus resulting as image streaks that are supposed to be aligned with the mean local sea surface wind field (Du et al., 2002; Horstmann et al., 2002; Schiavulli et al., 2011). Based on this rationale, the proposed approach aims at providing the wind direction estimation at sea by simply retrieving the orientations of these wind-induced phenomena. In fact, the DWT-MRA approach allows obtaining wind direction information by analyzing the SAR imagery at different scales, in both time and frequency domain (Mallat, 1989; Du et al., 2002; Schiavulli et al., 2011). The estimated wind direction presents an inherent 180° wind direction ambiguity, which can be properly solved either if wind shadowing is present in SAR imagery or by using external information, such as the ASCAT scatterometer data. The processing chain relevant to the SAR wind direction retrieval technique is detailed in (Du et al., 2002; Schiavulli et al., 2011).

3.2 The SWAN model

The wind-wave modeling used in this work is based on the SWAN model, a third-generation numerical wave model that allows computing random, short-crested waves in coastal regions with shallow water and ambient currents (Holthuisen et al., 1993; Booij et al., 1999; Benassai, 2006, Benassai and Ascione, 2006). It describes the temporal and spatial variation of the wind-induced surface elevation, the white-capping effects and the friction with the sea bottom layer (Holthuisen et al., 1993; Booij et al., 1999; Benassai, 2006, Benassai and Ascione, 2006). In the SWAN model, the waves are described with the two-dimensional wave action density spectrum $N=F/\sigma$ (F is the spectrum and σ is the intrinsic frequency) even when non-linear phenomena dominate (e.g., in the surf zone). The action density spectrum N is

considered rather than the energy density spectrum $E(\sigma, \theta)$, since in the presence of ambient currents only the action density is conserved (Whitham, 1974). The evolution of the wave spectrum is described by the spectral action balance equation (Hasselmann et al., 1973):

$$\frac{\partial}{\partial t} N + \frac{\partial}{\partial x} c_x N + \frac{\partial}{\partial y} c_y N + \frac{\partial}{\partial \sigma} c_\sigma N + \frac{\partial}{\partial \theta} c_\theta N = \frac{S}{\sigma} \quad , \quad (2)$$

where S is the source function representing the sum of wave energy input from wind, energy dissipation by wave breaking and the energy redistribution of energy via non-linear interaction between frequency components. The first term on the left-hand side of Eq. (2) represents the timely-change rate of the local action density spectrum. The second and third term on the left-hand side of Eq. (2) represents the propagation of the action density spectrum in the Cartesian coordinates space, with propagation velocities c_x and c_y . The fourth term on the left-hand side of Eq. (2) represents the shifting of the relative frequency in the action density spectrum due to variations in depths and currents, with a propagation velocity c_σ . The fifth term on the left-hand side of Eq. (2) represents both the depth- and the current-induced refraction of the local action density spectrum, with propagation velocity c_θ . The term at the right-hand side of the action balance Eq. (2) is the source term of the energy density, representing the effects of generation, dissipation, and non-linear wave-wave interactions.

The SWAN model is operational at Dipartimento di Scienze Applicate (DSA) of the Università degli Studi di Napoli Parthenope since January 2005 and is adopted for simulating both waves generation and propagation in the Gulf of Naples. The model is typically forced using the wind field at 1-hour intervals provided by the Advanced Research Weather Research and Forecast (WRF-ARW) wind field model data, i.e. the next-generation mesoscale numerical weather model predictions that are designed to serve both operational forecasting and atmospheric research needs (Holthuisen et al., 1993; Booij et al., 1999; Benassai, 2006; Benassai and Ascione, 2006). The model is implemented on nested grids, with an implicit numerical propagation scheme, that makes the numerical code quite effective in shallow water (Holthuisen et al., 1993; Booij et al., 1999; Benassai, 2006; Benassai and Ascione, 2006). Outputs of the SWAN model include significant wave height (H_s) on gridded fields, with the associated wave directions (D_w) and periods (T_p), and the wave energy spectral information at different wavelengths.

3.3 The CVA model

The CVA approach used in this paper is based on the methodology first proposed in (Benassai et al., 2009), where a new key parameter known as impact index I_i is defined for the coastal flooding risk evaluation. This parameter accounts for wave climate, bathymetry and sediment data and depends on the wave run-up height, the seasonal and long-term erosion index, and the efficiency of coastal protection structures. It is given by (Benassai et al., 2009):

$$I_i = I_{Ru} + I_R + I_D + E + T \quad , \quad (3)$$

where I_{Ru} is an inundation distance index associated to the wave run-up, I_R is the short-term erosion index for the shoreline, I_D is the index of stability for backshore coastal protection structures, E is the long-term erosion index and T is the tidal range. Compared to the main CVA methods, this methodology can be applied on a small geographical scale for coastal flooding risk evaluation. Moreover, it must be noted that the tidal effects are not considered in (Benassai et al. 2009) since the application is relevant to the Mediterranean Sea, i.e. a micro-tidal environment.

Here, the CVA is carried out by evaluating Eq. (3), without considering I_D and T index contributions. In fact, the test area (i.e. the Southern Tyrrhenian Coastal Sea basin) is a micro-tidal coastal environment (hence, $T = 0$), where no coastal protection is present (hence, $I_D = 0$). Therefore, only I_{Ru} , I_R and E contributions will be taken into account for the evaluation of I_i .

The I_{Ru} index provides the measurement of the potential inundation capacity, which characterizes natural beaches with respect to wave storms. I_{Ru} assumes values, which depend on the percentage associated to the maximum horizontal wave run-up distance on the beach (X_{max}) normalized with respect to the emerged beach width (L) (Benassai et al., 2009). X_{max} is retrieved through the wave run-up height, which depends on both beach and wave properties:

$$X_{max} = \frac{R_{2\%}}{tg(\beta)} \quad , \quad (4)$$

where β is the tidal beach slope and $R_{2\%}$ is the 2% exceedance level for wave run-up peaks. The latter is retrieved through the empirical approach proposed in (Stockdon et al., 2006):

$$R_{2\%} = 1.1 \cdot \left(0.35 \cdot \beta_f \cdot \sqrt{(H_0 \cdot L_0)} + \frac{\sqrt{H_0 \cdot L_0 \cdot (0.563 \beta_f^2 + 0.004)}}{2} \right) \quad , \quad (5)$$

where β_f is the foreshore beach slope defined over the area of significant swash activity (it is approximated to β), H_0 is the foreshore wave height (it can be approximated to H_s) and L_o is the foreshore wave length evaluated as function of Tp (Benassai et al., 2009).

Based on Eq.(s) (4) and (5) and according both to X_{max} and L estimates, I_{Ru} values can be customary clustered in four discrete levels (Benassai et al., 2009):

$$I_{Ru} = \begin{cases} 1 & \text{if } \frac{X_{max}}{L} \% < 40 \\ 2 & \text{if } 40 \leq \frac{X_{max}}{L} \% < 60 \\ 3 & \text{if } 60 \leq \frac{X_{max}}{L} \% < 80 \\ 4 & \text{if } \frac{X_{max}}{L} \% \geq 80 \end{cases}, \quad (6)$$

where I_{Ru} values are mapped into four categories of the short-term vulnerability according to the classification rule defined in (Benassai et al., 2009), i.e. stable ($I_{Ru} = 1$), low ($I_{Ru} = 2$), moderate ($I_{Ru} = 3$) and high ($I_{Ru} = 4$) short-term erosion of the natural beach (see Table I).

The I_R index provides a measurement of potential beach retreat and is used for the dynamical calculation of the shoreline retreat based on the convolution method of Kriebel & Dean (1993). I_R values depend on the percentage associated to the maximum beach retreat (R_{max}) normalized with respect to L (Benassai et al., 2009). R_{max} is evaluated as the maximum value of the general solution associated to the Kriebel & Dean convolution method (1993):

$$\frac{R(t)}{R_{\infty}} = \frac{1}{2} \left\{ 1 - \frac{\gamma^2}{1+\gamma^2} \exp(-2\sigma t/\gamma) - \frac{1}{1+\gamma^2} [\cos(2\sigma t) + \gamma \sin(2\sigma t)] \right\}, \quad (7)$$

where:

$$R_{\infty} = S \frac{W_b - d_b/m_0}{B + d_b - S/2}. \quad (8)$$

S is the sea level increase due to the wave storm (it is directly proportional to H_s), B is the berm height, m_0 is the foreshore seabed slope, d_b is the breaking depth (it is directly proportional to H_s), W_b is the offshore breaking depth distance (it is inversely proportional to the median dimension of beach sediments μ_s), σ is the angular frequency associated to the

1 wave period T_p , γ is the ratio between the beach system time scale T_s and the wave storm
 2 duration T_D (Benassai et al., 2009).

3 Based on Eq.(s) (7) and (8) and according to both R_{max} and L estimates, I_R values can be
 4 customary clustered in four discrete levels (Benassai et al., 2009):

$$5 \quad I_R = \begin{cases} 1 & \text{if } \frac{R_{max}}{L} \% < 40 \\ 2 & \text{if } 40 \leq \frac{R_{max}}{L} \% < 60 \\ 3 & \text{if } 60 \leq \frac{R_{max}}{L} \% < 80 \\ 4 & \text{if } \frac{R_{max}}{L} \% \geq 80 \end{cases}, \quad (9)$$

6 where I_R values are properly mapped into four categories of the short-term vulnerability
 7 according to the classification rule defined in (Benassai et al., 2009), i.e. stable ($I_R = 1$), low
 8 ($I_R = 2$), moderate ($I_R = 3$) and high ($I_R = 4$) short-term erosion of natural beach (see Table 1).

9 The E index provides the long-term evaluation of potential beach retreat and is measured by
 10 comparing photogrammetric flights of different years relevant to the observed test area. It
 11 assumes values, which depend on the beach erosion rate V_E (m/yr) (Benassai et al., 2009):

$$12 \quad E = \begin{cases} 1 & \text{if } V_E (m / yr) < 0.5 \\ 2 & \text{if } 0.5 \leq V_E (m / yr) < 1 \\ 3 & \text{if } 1 \leq V_E (m / yr) < 2 \\ 4 & \text{if } V_E (m / yr) \geq 2 \end{cases}, \quad (10)$$

13 where E values are properly mapped into four categories of the long-term vulnerability
 14 according to the classification rule defined in (Benassai et al., 2009), i.e. stable ($E = 1$), low (E
 15 $= 2$), moderate ($E = 3$) and high ($E = 4$) long-term erosion of the natural beach (see Table 1).

16 Based on the definition of both short- and long-term erosion indexes, the impact index I_i is
 17 evaluated according to Eq. (3). Based on the customary classification of I_{Ru} , I_R and E
 18 parameters, I_i values are mapped into four categories of coastal vulnerability risk according to
 19 the classification rule defined in (Benassai et al., 2009), i.e. stable ($I_i = 3$), low ($3 < I_i \leq 6$),
 20 moderate ($6 < I_i \leq 9$) and high ($9 < I_i \leq 12$) vulnerability risk of natural beach (see Table 1).

4 Experimental results

In this section, some meaningful experimental results are presented and discussed to show the benefits of X-band CSK© SAR measurements to provided valuable sea surface wind field estimations for the improvement of both wind-wave modeling and coastal vulnerability assessment. They are relevant to the application of the SWAN model in a coastal environment and the subsequent assessment of the coastal vulnerability, with forcing provided by X-band CSK© SAR-derived wind field estimations.

4.1 SAR wind field retrieval

First of all, a preliminary analysis on the effectiveness of the X-band SAR wind field retrieval approach is undertaken by using X-band CSK© SAR measurements described in Section 2.

A SAR-based wind field retrieval gridding scale of $12.5\text{km} \times 12.5\text{km}$ is considered along with the azimuth and range directions. The ground truth used for comparison and validation purposes is provided by timely and spatially co-located $12.5\text{km} \times 12.5\text{km}$ ASCAT scatterometer wind fields. In the particular case where the ASCAT scatterometer wind field is not available for the SAR acquisition, the reference ground truth is then provided by $28\text{km} \times 20\text{km}$ ECMWF model data. To properly co-locate the reference ground truth and the SAR-based wind field estimation, both a linear interpolation in time and a bi-linear spatial interpolation onto the SAR-based wind field retrieval gridding scale is accomplished.

A single experiment is fully detailed to demonstrate the consistency of the X-band CSK© SAR-derived wind field retrieval, taking full benefits of VV-polarized Level 1B DGM ScanSAR Huge Region mode CSK© SAR data.

The experiment is relevant to the X-band CSK© SAR acquisition of 17 December 2010 at 18:00 UTC, which refers to an interesting winter wave storm occurred in the Tyrrhenian Sea coastal area on 2010. The VV-polarized NRCS image is shown in gray tones in Fig. 1(a), where the scalloping effect and weak atmospheric phenomena are present. The output of the pre-processing step is shown in Fig. 1(b), where the land is masked out. It must be noted that SAR image quality is improved both by reducing the scalloping effect and by filtering out atmospheric phenomena.

The output of the wind speed retrieval is shown in Fig. 2(a) together with the reference timely and spatially co-located ECMWF and ASCAT ground truth (see Fig. 2(b)-(c), respectively). It

must be noted that in this particular case, the ASCAT scatterometer ground truth does not cover the whole spatial domain of the SAR acquisition (see Fig. 2(c)-(d)). The comparison between the SAR-based wind speed estimation and the reference ground truth (both the scatterometer- and the model-based wind speed) shows a fair agreement with root mean square error (RMSE) values lower than 3m/s. In fact, the CSK©SAR-ASCAT and CSK©SAR-ECMWF wind speed inter-comparisons provide RMSE values equal to 0.96m/s and 1.9m/s, respectively. Experimental results demonstrate that the X-band CSK© SAR wind speed estimations provided at the gridding scale of 12.5km×12.5km are consistent and effectively comparable with the reference ground truth. This result further demonstrates the physical soundness of the SAR-based wind speed retrieval approach showing the effectiveness of the X-band Azimuth cut-off model function. However, it can be noted that non-negligible differences in terms of sea surface wind speed are present closer to the coastal area of SAR image domain, for both ECMWF and ASCAT scatterometer winds. This could be explained by taking into account that both the reference ASCAT scatterometer and ECMWF model wind speeds are available at the resolution gridding scale of 12.5km×12.5km and 28km×20km, respectively.

The output of the SAR-based wind direction retrieval is shown in Fig. 3(a)-(b), together with the timely and spatially co-located ECMWF and ASCAT scatterometer-based wind direction, respectively. The comparison between the SAR-based wind direction estimation and the reference ground truth (both the scatterometer- and the model-based wind direction) shows a fair agreement with RMSE values equal to 6° and 12° for the CSK©SAR-ASCAT and the CSK©SAR-ECMWF wind direction inter-comparisons, respectively. Experimental results agree with previous ones, demonstrating that some of the differences observed between the reference ground truth and the X-band SAR-based DWT-MRA wind direction retrievals can be explained by considering the different spatial gridding resolution scale of both modeled (ECMWF) and remotely sensed (SAR and ASCAT) wind direction estimation products.

Other results are summarized in the scatter plots of Figs. 4, where the 12.5km×12.5km SAR-based wind speed and wind direction retrievals are compared with respect to the ASCAT scatterometer reference wind speed and wind direction, respectively, for the whole processed CSK© SAR data set. The comparison between the X-band SAR-based wind field retrievals and ECMWF model winds will be presented in the next section in terms of sea wave numerical simulations. Experimental results agree with the previous thus demonstrating the

consistency of SAR-derived wind field estimations with respect to the ASCAT scatterometer reference ground truth. In detail, the CSK© SAR-ASCAT wind speed inter-comparison (see Fig. 4(a)) provides a mean error (μ) value of -0.73m/s , a standard deviation (σ) value of 2.07m/s and an RMSE value of 2.19m/s . On the other side, the CSK© SAR-ASCAT wind direction inter-comparison (see Fig. 4(b)) provides a μ value of 1.71° , a σ value of 18.88° and an RMSE value of 18.95° . These results demonstrate the consistency of X-band SAR-derived wind field retrievals with respect to the ASCAT scatterometer ground truth. This latter suffers from uncertainty over the maritime coastal areas and it is not able to capture small-scale features, which can in turn be revealed by means of SAR data. Such results demonstrate the effectiveness of both the X-band Azimuth cut-off model function and the DWT-MRA technique presented in Section 2.1 to get consistent wind speed and wind direction estimation, respectively, even through X-band SAR data. Furthermore, experimental results show the full benefits of X-band Level 1B DGM ScanSAR Huge Region mode CSK© SAR data as alternative source of wind field estimation.

In summary, the wind speed is retrieved with a RMSE value of about 2m/s and this result is in agreement to what experienced in C-band azimuth cut-off literature (Chapron et al., 1995; Kerbaol, 1998; Korsbakken et al., 1998). The wind direction is retrieved with a RMSE value lower than 20° and this result is in total accordance with the relevant literature (Du et al., 2002; Horstmann et al., 2002; Schiavulli et al., 2011).

4.2 Sea wave numerical simulations

In this sub-section, sea wave numerical simulations accomplished through the SWAN model are described with respect to some relevant wave storms recorded in the considered test area during the winter season of 2010 (see Table 2). In all the experiments, H_s and T_D are used as reference parameter at the output of the SWAN simulations. The latter are properly undertaken by using different wind field forcings, i.e. ECMWF model winds, SAR-based wind field estimations and ECMWF-SAR blended wind field products. For comparison purposes, buoys-derived data are used as reference ground truth information.

The first experiment is relevant to the wave storm of 8-10 November 2010, which exhibits the maximum time evolution ($T_D = 55\text{h}$) with respect to the other storms and is associated to a strong atmospheric perturbation (see Table 2). The H_s values, obtained by forcing the SWAN model with the above-mentioned wind field products, are plotted against the time evolution of

the wave storm (see Fig. 5). A first visual analysis shows that the H_s profile obtained with ECMWF model winds (blue line) does not fit the reference buoys one (red line), with a strong H_s overestimation (38%) over the correctly retrieved time evolution of the storm ($T_D = 55h$). Conversely, the H_s profiles obtained with SAR-derived wind field estimations (green line) and ECMWF-SAR blended wind field products (black line) well fit the reference buoys one, providing a correct retrieval of the storm evolution (see T_D values in Table 2). In detail, the ECMWF-SAR blended wind field product exhibits a smaller H_s underestimation (9%) with respect to the SAR one (40%). A deeper analysis (see Table 2) shows that the maximum H_s value obtained by using ECMWF model winds (blue line) and SAR-based wind field estimations (green line) is overestimated ($H_s = 5.5m$) and underestimated ($H_s = 2.4m$), respectively, with respect to the reference buoy data ($H_s = 4.23m$). Conversely, a much better accordance is experienced with the ECMWF-SAR blended wind field product ($H_s = 3.5m$, see the black line). This latter result takes into account that ECMWF model winds cover a wide spatial domain with dense temporal sampling, while SAR-derived wind field estimations are sample local measurements obtained over a wide spatial domain. Since the dense temporal sampling of wind field forcing is necessary to get reliable SWAN simulation results, it is mandatory to provide denser temporal SAR-based wind field estimations. As a matter of fact, the ECMWF-SAR blended wind field product is here provided as the most straightforward solution to overcome the problem in question. In detail, experimental results demonstrate the effectiveness of the ECMWF-SAR blended wind field product for a suitable description of the wave storm in terms of H_s and T_D , see Table 3.

The second experiment is relevant to the wave storm of 17-18 December 2010, which exhibits the maximum wave height ($H_s = 5.01m$) and the minimum time evolution ($T_D = 24h$) among the other wave storms (see Table 2 and Fig. 6). The H_s values, obtained by forcing the SWAN model with the above-mentioned wind field products, are plotted against the time evolution of the wave storm (see Fig. 6). A first visual analysis shows that the H_s profiles obtained with the three above mentioned wind field forcings well fit the reference one (red line). A deeper analysis shows that ECMWF model winds (blue line) are in perfect agreement with the reference buoys data (red line), in terms of both the maximum H_s value ($H_s = 5m$) and wave storm time evolution ($T_D = 24h$). Conversely, SAR-based wind field estimations (green line) and ECMWF-SAR wind field products (black line) exhibit a general H_s underestimation with respect to the reference buoys data (blue line), although they are both able to correctly retrieve the time evolution of the storm (see T_D values in Table 2). In detail,

the maximum H_s values obtained through SAR ($H_s = 2.5\text{m}$) and ECMWF-SAR blended wind field products ($H_s = 3.4\text{m}$) demonstrates a smaller H_s underestimation for the ECMWF-SAR blended product (32%) with respect the SAR one (50%), see Table 3. This result is most likely due both to the faster time evolution of the wave storm with respect to the previous wave storm and to the underestimation of SAR-based wind field retrievals. However, experimental results demonstrate the effectiveness of the ECMWF-SAR blended wind field product for a suitable description of the wave storm in terms of H_s and T_D values, see Table 3.

The third experiment is relevant to the wave storm of 23-25 December 2010, which exhibits a maximum H_s value equal to 4.29m and a time evolution T_D of 48h (see Table 2). The H_s values, obtained by forcing the SWAN model with the above-mentioned wind field products, are plotted against the time evolution of the wave storm (see Fig. 7). Experimental results show that the H_s profiles obtained with the three above mentioned wind field forcings well fit the reference buoys one (red line) and are able to catch the maximum energetic peak of the storm, see Fig. 7. In detail, ECMWF model winds (blue line) provide a consistent H_s retrieval ($H_s = 4\text{m}$) with respect to the reference buoys one, although they exhibit a slight T_D overestimation (9%). Conversely, SAR-derived wind field estimations (green line) and ECMWF-SAR blended wind field products (black line) exhibit a significant (44%) and slight (20%) H_s underestimation, respectively, although they are both able to retrieve the time evolution of the storm (see T_D values in Table 2). Again, experimental results demonstrate the effectiveness of the ECMWF-SAR blended wind field product for a suitable description of the wave storm in terms of H_s and T_D profiles.

In summary, all the experimental results demonstrate the benefits of the ECMWF-SAR blended wind field product, which can retrieve SWAN-based wind-wave interaction parameters for the effective wave storm description, in terms of time evolution T_D and maximum H_s value.

4.3 CVA Experiments

In this sub-section, some meaningful CVA results are discussed with respect to the three relevant wave storms described in Table 2. The reference test area is the Sele coastal plain, which has shown a high sensitivity to major flood risk as reported in (Alberico et al., 2012).

Based on the SWAN simulating results described in the sub-section 4.2, the CVA is here accomplished by evaluating I_{Ru} , I_R , E and I_i through the SWAN-based wind-wave interaction parameters that have been retrieved by using both ECMWF model winds and ECMWF-SAR blended wind field products. For comparison purposes, buoys-derived information is used, together with the coastal wave climate and the morpho-sedimentary features of the interested area, to retrieve reference I_{Ru} , I_R , E and I_i profiles (Di Paola, 2011; Alberigo et al., 2012).

Firstly, a brief analysis of the Sele Coastal plain is provided with respect to some meaningful coastal morpho-sedimentary features. In Fig. 8, the elevation map of the test area is shown in gray tones together with the position of ten specific elevation transects (from P1 to P10), each of ones encompasses the intertidal and emerged beach elevation as shown in Fig. 9. The longitudinal extensions of the beach are given in Table 3 together with both their relative percentage value and their longitudinal extensions. The low coastline under study presents different morphological and anthropic features, which allow distinguishing some different stretches of coastline (see Tables 3 and 4): 1) the first one, extending from the mouth of river Picentino till the river Asa (P1 and P2 transects), shows small beaches and strong urbanization, with gravely ($\mu_s=5.037\text{mm}$) and sandy ($\mu_s=0.971\text{mm}$) sediments for P1 and P2 transects, respectively. These profiles are classified as medium ($20<L<50$) and restricted ($L<20$) emerged beach for about 48% (1,200m) and 52% (1,300m) of their total extension (2,500m), respectively; 2) the second one, around the mouth of the river Tusciano, is characterized by a well preserved and stable dune system (P3 and P4 transects), with sandy ($\mu_s=0.753\text{mm}$) and finer sandy ($\mu_s=5.037\text{mm}$) sediments for P3 and P4 transects, respectively (see Table 4). These profiles are classified as wide ($L>50$) and medium ($20<L<50$) emerged beaches for about 32% (800m) and 68% (1,700m) of their total extension (2,500m), respectively (see Table 3); 3) the third one, i.e. the area between the mouths of rivers Tusciano and Sele (P5 and P6 transects), is characterized by eroded and deteriorated dunes, with gravely ($\mu_s=4.487\text{mm}$) and finer sandy ($\mu_s=0.444\text{mm}$) sediments for P5 and P6 transects, respectively (see Table 4). On the left bank of river Sele, an intense anthropogenic load is also experienced (P7 transect), which is characterized by finer sandy ($\mu_s=0.444\text{mm}$) sediments (see Table 4). These profiles are classified as medium ($20<L<50$) and restricted ($L<20$) emerged beach for about 82% (2,050m) and 14% (350m) of their total extension (2,500m), respectively, with the presence of defense works for the remaining 100m (4%), see Table 3; 4) the fourth one, which extends from the cities of Paestum and Agropoli (P8, P9 and P10 transects), is characterized by wider beaches with both well preserved dunes and low

anthropic load. These profiles exhibit fine sandy sediments (μ_s is equal to 0.341mm, 0.396mm and 0.346mm for P8, P9 and P9 transects, respectively) and are classified as wide ($L>50$) and medium ($20<L<50$) emerged beaches for about 60% (1,200m) and 40% (800m) of their total extension (2,500m), respectively (see Tables 3 and 4).

Based on the description and the classification of the morpho-sedimentary features of the test area (see Tables 3 and 4), I_{Ru} , I_R , E and I_i profiles are evaluated over the ten transects in Fig.(s) 8 and 9, according to the CVA approach described in Section 3.3. First of all, experimental results relevant to the reference buoys data are discussed to provide the reference vulnerability information for the considered transects. Then, a comparative analysis is presented with respect to the reference buoys data to analyze the performances of both ECMWF model winds and ECMWF-SAR blended wind field products for CVA purposes.

In Fig. 10 the X_{max}/L % profile, obtained through the reference buoys data (purple bars), the ECMWF model winds (red bars) and the ECMWF-SAR blended wind field product (yellow bars), is shown together with the associated I_{Ru} values for the three reference wave storms. As clearly shown by the reference buoys data (purple bars), the lowest X_{max}/L % values are experienced for P8-P9-P10 transects that correspond to the areas with greater L values (see Table 4). This result highlights the stronger impact of L with respect to β_f (here approximated to β) for the evaluation of X_{max}/L % and X_{max} , respectively. In fact, on one side, X_{max}/L % is inversely proportional to L , therefore it is minimum for the maximum L values, which correspond to P8, P9 and P10 transects (see Table 4). On the other side, X_{max} is inversely proportional to β , therefore it is minimum for the maximum β values, which correspond to P4, P6 and P10 transects (see Table 4). In addition to this, it can be noted that X_{max}/L % is greater from P1 to P7 transects with the maximum value reached at P7 beach profile, which exhibits the lowest L value and therefore represents the most critical case in terms of short-term vulnerability risk (see Table 4). Experimental results show that the X_{max}/L % profile is the same for the three reference wave storms (see Fig. 10). In detail, the most pronounced results are experienced for the second storm (see Fig. 10(b)), which exhibits the greatest H_s value among the three wave storms. This result shows the key-role played by H_s for the evaluation of X_{max} , which reaches the maximum for the greatest retrieved H_s value.

Based on the classification rule defined for I_{Ru} (see section 3.3) and according to the X_{max}/L % values obtained for the three reference wave storms, it is possible to define the short-term vulnerability risk associated to I_{Ru} , for each transect of the considered test area. In detail, with

respect to the first and the third wave storms, a stable ($I_{Ru} = 1$), low ($I_{Ru} = 2$), medium ($I_{Ru} = 3$) and high ($I_{Ru} = 4$) short-term vulnerability risk is experienced for P10, P8-P9, P2-P4-P6 and P1-P3-P5-P7 transects, respectively. With respect to the second wave storm, a low ($I_{Ru} = 2$), medium ($I_{Ru} = 3$) and high ($I_{Ru} = 4$) short-term erosion value is experienced for P9-P10, P8 and P1-P2-P3-P4-P5-P6-P7 transects, respectively. All the results demonstrate that P7 is the most critical case among the ten considered transects, since it exhibits the highest X_{max}/L % value and then is the most exposed beach profile in term of short-term vulnerability risk.

Following this preliminary analysis, the comparison between the reference buoys data (purple bars) and both ECMWF (red bars) and ECMWF-SAR blended wind field products (yellow bars) is properly discussed, see Fig. 10. On one side, it can be noted that the X_{max}/L % profile and the corresponding I_{Ru} values, obtained through ECMWF model winds for the ten considered transects, are in perfect agreement with the reference buoys data (purple bars) for the second and the third wave storms. Conversely, a non-negligible overestimation (30%) of both X_{max}/L % profile and therefore I_{Ru} values is experienced with respect to the first wave storm. These results take into account that ECMWF model winds correctly retrieve the maximum H_s value for the second and the third wave storms, with a pronounced H_s overestimation for the first wave storm (see Section 4.2). On the other side, it can be noted that the X_{max}/L % profile and the corresponding I_{Ru} values, obtained through ECMWF-SAR blended wind field products for the ten considered transects (yellow bars), well fit the reference buoys data for the first and the third wave storms, with a non-negligible disagreement for the second one. In detail, a pronounced X_{max}/L % underestimation (30%) is provided for the second wave storm, which severely impacts the I_{Ru} evaluation thus providing underestimated short-term vulnerability risk values. Conversely, a slight X_{max}/L % underestimation (15%) is provided for the third wave storm, which does not impact the evaluation of I_{Ru} index. These results take into account that ECMWF-SAR blended wind field products correctly retrieve the maximum H_s value for the first wave storm, with an H_s underestimation for the second and the third wave storms (see Section 4.2).

In Fig. 11 the R_{max}/L % profile, obtained through reference buoys data (purple bars), ECMWF model winds (red bars) and ECMWF-SAR blended wind field product (yellow bars), is shown together with the associated I_R values for the three reference wave storms. As clearly shown by the reference buoys data (purple bars), the lowest values of R_{max}/L % are experienced for P1 and P5 transects that correspond to the areas where the beach sediments

show the greater μ_s values (see Table 4). This result takes into account that R_{max} is inversely proportional to μ_s , which plays a key role for the evaluation of both T_s and W_b within Eq. (7). Moreover, it can be noted that R_{max}/L % profile is the same for all the three reference wave storms. The most pronounced results are obtained for the second wave storm, which exhibits both the greatest H_s and the lowest T_D values (see Table 2). This result takes into account that R_{max} is directly proportional to H_s and inversely proportional to T_D , see Eq.(s) (7) and (8). In fact, on one side, high H_s values provide high S , d_b and then R_{max} values. On the other side, low T_D value provides the reduction of γ , which in turn provides high R_{max} values. This means that for a given H_s value, wave storms with lower T_D value exhibit higher R_{max}/L % profiles. In addition to this, it is shown that, for the three reference wave storms, the maximum R_{max}/L % value is experienced at P7 beach profile, which both exhibits the lower L values among the ten considered transects and therefore represents the most critical case in terms of short-term vulnerability risk (see Table 4). This result highlights the impact of L for the evaluation of R_{max}/L %.

Based on the classification rule defined for I_R (see section 3.3) and according to the R_{max}/L % values experienced for the three reference wave storms, it is possible to define the short-term vulnerability risk associated to I_R , for each transect of the considered test area. With respect to the first and the third wave storms, a stable ($I_R = 1$), low ($I_R = 2$), medium ($I_R = 3$) and high ($I_R = 4$) short-term vulnerability risk is experienced for P1-P5-P9, P2-P8, P3-P4-P10 and P6-P7 transects, respectively. With respect to the second wave storm, a stable ($I_R = 1$), low ($I_R = 2$), medium ($I_R = 3$) and high ($I_R = 4$) short-term vulnerability risk is experienced for P1-P5, P9, P2-P8 and P3-P4-P6-P7-P10 transects, respectively. All the results clearly show that P7 is the most critical case among the ten considered transects, since it exhibits the highest R_{max}/L % value and then is the most exposed beach profile in term of short-term vulnerability risk.

Following this preliminary analysis, the comparison between the reference buoys data (purple bars) and both ECMWF (red bars) and ECMWF-SAR blended wind field products (yellow bars) is properly discussed, see Fig. 11. Experimental results agree with the ones obtained for X_{max}/L %. On one side, ECMWF model winds exhibit a good agreement with the reference buoys data for the second and the third wave storms, while a pronounced overestimation (100%) is provided for the first wave storm. This result takes into account the H_s overestimation provided by ECMWF model winds for the first wave storm (about 30%), which in turn provides overestimated R_{max}/L and short-term vulnerability risk values. On the

other side, ECMWF-SAR blended wind field products exhibit a good agreement with the reference buoys data for the first wave storm, while they underestimate both R_{max}/L % and I_R values for the second (50%) and the third (10%) wave storms. This result takes into account the H_s underestimation provided by ECMWF-SAR blended wind field products for the second and the third first wave storms, which in turn provides underestimated R_{max}/L % and short-term vulnerability risk values.

In Table 4, the V_E profile, obtained through the long-term photogrammetric analysis, is shown together with E values for each transect of the considered test area. Experimental results show that a stable ($E = 1$), low ($E = 2$), medium ($E = 3$) and high ($E = 4$) long-term vulnerability risk is experienced for P8-P9-P10, P1-P2, P3-P4 and P5-P6-P7 transects, respectively.

In Fig. 12, the impact index I_i and the coastal vulnerability risk classification, obtained through reference buoys data (purple bars), ECMWF model winds (red bars) and ECMWF-SAR blended wind field product (yellow bars), is shown for the three reference wave storms. As clearly shown by the reference buoys data (purple bars), the first and the third wave storms exhibit a low ($4 \leq I_i \leq 6$), moderate ($7 \leq I_i \leq 9$) and high ($10 \leq I_i \leq 12$) vulnerability risk for P8-P9-P10, P1-P2-P4-P5 and P3-P6-P7 transects, respectively. With respect to the second wave storm, a low ($4 \leq I_i \leq 6$), moderate ($7 \leq I_i \leq 9$) and high ($10 \leq I_i \leq 12$) vulnerability risk is experienced for P9, P1-P8-P10, P2-P3-P4-P5-P6-P7-P9 transects, respectively. All the experimental results clearly show that P7 is the most critical case among the ten considered transects, since it exhibits the highest I_i value and then is the most exposed beach profile in term of coastal vulnerability risk.

Following this preliminary analysis, the comparison between the reference buoys data (purple bars) and both ECMWF (red bars) and ECMWF-SAR blended wind field products (yellow bars) is properly discussed, see Fig. 12. On one side, ECMWF model winds exhibit a good agreement with the reference buoys data for the second and the third wave storms, while a slight overestimation (15%) is observed for the first wave storm. On the other side, ECMWF-SAR blended wind field products exhibit a good agreement with the reference buoys data for the first and the third wave storm, while they underestimate I_i values for the second (15%) wave storm. These results take into account both the SWAN simulating results described in Section 4.2 and the short-term coastal vulnerability analysis provided in terms of I_{Ru} and I_R profiles. Experimental results clearly show that the I_i overestimation (underestimation) provided by ECMWF (ECMWF-SAR blended) wind field products is always lower than the

one experienced for I_{Ru} and I_R profiles. This result takes into account that I_i is evaluated over a certain range of values associated to both short- (I_{Ru} and I_R) and long-term (E) erosion indexes. Therefore, it allows consistently reducing the differences experienced for each single considered index, especially for I_{Ru} and I_R .

In summary, experimental results demonstrate the benefits of the ECMWF-SAR blended wind field product, which allows consistently retrieving short-term (I_{Ru} and I_R) and long-term (I_i) vulnerability risk parameters for the effective CVA analysis of the considered test area.

5 Conclusions

In this paper, the capabilities of CSK© SAR data are first investigated to provide surface wind fields for the improvement of wind-wave modeling and coastal vulnerability assessment purposes. The SAR data set consists of 60 X-band VV-polarized Level 1B DGM ScanSAR Huge Region CSK© SAR measurements, collected in the test area of the southern Tyrrhenian Sea basin during the winter season of 2010. The SAR-based wind speed estimation is provided by means of the azimuth cut-off procedure, while the SAR-based wind direction retrieval is achieved by using the DWT-MRA approach. The wind-wave modeling is based on the third-generation SWAN model, while the CVA is provided by means of a key parameter known as impact index (I_i). Experimental results have shown that:

- X-band CSK© SAR data can be effectively used as alternative resource to retrieve the wind field information at the sea surface. The consistency of X-band CSK© SAR-derived wind field retrievals is validated with respect to the ASCAT scatterometer ground truth. Experimental results demonstrate the effectiveness of the azimuth cut-off procedure and the DWT-MRA technique to retrieve the sea surface wind speed and wind direction with RMSE values of about 2m/s and 20°, respectively.
- SWAN numerical simulations are run with respect to three reference winter wave storms of 2010, where three different wind field forcing (e.g. ECMWF, SAR and ECMWF-SAR blended winds) are effectively used to describe the wave storm events in terms of H_s and T_D profiles. The consistency of wind field forcings is validated with respect to National and Regional buoy-derived information. Experimental results demonstrate the benefits of the ECMWF-SAR blended wind field product, which can

1 retrieve SWAN-based wind-wave interaction parameters, with a slight H_s
2 underestimation at the storm peak (9-30%).

- 3 • CVA is accomplished with respect to the three above-mentioned wave storms along
4 ten beach profiles of the Sele coastal plain. Some meaningful vulnerability indexes
5 (i.e. I_{Ru} , I_R , E and I_i) are evaluated through the SWAN-based wind-wave interaction
6 parameters that have been retrieved by using both ECMWF model winds and
7 ECMWF-SAR blended wind field products. The consistency of these two wind field
8 products is validated with respect to buoys-derived information. Experimental results
9 demonstrate the benefits of the ECMWF-SAR blended wind field product, which
10 allows retrieving short-term (I_{Ru} and I_R) and long-term (I_i) vulnerability risk
11 parameters for the effective CVA of the considered test area. Although ECMWF-SAR
12 blended wind field product generally underestimates I_{Ru} (15-30%) and I_R (10-50%)
13 profiles, they provide a slight I_i underestimation (15%) that does not affect the
14 vulnerability risk classification of the interested coastal area.

15 Despite the limitations of dense temporal CSK© SAR acquisitions (and then SAR-derived
16 wind field products), experimental results show that CSK© SAR-based wind field retrievals
17 represents a valuable tool to improve coastal wind-wave modeling, for both sea-wave and
18 CVA purposes.

20 **Acknowledgements**

21 COSMO-SkyMed© SAR data used in this study are provided by Italian Space Agency under
22 the scientific research project entitled “Improvement of Oceanic Modeling for Coastal
23 Management by means of COSMO-SkyMed© SAR data” (Project ID 1500). Authors would
24 like to acknowledge Dr. Di Paola for beach morphological data and useful discussions.

References

- Alberico, I., Amato, V., Aucelli, P. P. C., Di Paola, G., Pappone, G. and Roszkopf, C.M.: Historical and recent changes of the Sele River coastal plain (Southern Italy): natural variations and human pressures. *Rendiconti Lincei*, 23(1), 3-12, doi: 10.1007/s12210-011-0156-y, 2012.
- Benassai, G.: Introduction to coastal dynamics and shoreline protection, Wit Press, Southampton, 1, 1-356, ISBN: 1-84564-0543, 2006.
- Benassai, G., and Ascione, I: Implementation and validation of wave watch III model offshore the coastlines of Southern Italy, in: Proceedings of 25th International Conference on Offshore Mechanics and Arctic Engineering 2006- 92555, Hamburg, Germany, 4-9 June 2006, 553-560, 2006.
- Benassai, G., Chirico, F., and Corsini, S.: Una metodologia per la definizione del rischio da inondazione costiera, *Studi Costieri*, 16, 51-72, 2009.
- Booij, N., Ris, R. C., and Holthuijsen, L. H.: A third-generation wave model for coastal regions, Part I: Model description and validation, *J. Geophys. Res.*, 104, 7649-7666, 1999.
- Bruun, P.: Sea level rise as a cause of shore erosion, *J. WATERW PORT C-ASCE*, 88, 117-130, 1962.
- Carter, T. R., Parry, M. L., Nishioka, S., and Harasawa, H.: Technical guidelines for assessing climate change impacts and adaptation, University College London, London, and Centre for Global Environmental Research, Tskuba, Japan, 1994.
- Chapron, B., Fouhaily, T. E., and Kerbaol, V.: Calibration and validation of ERS wave mode products, *Inst. Fr. De Rech. pour l'Exploit. de la Mer*, Brest, France, Doc. DRO/OS/95-02, 1995.
- Diez, P.G., Perillo, G.M.E., and Picolo, M.C.: Vulnerability to seal-level rise on the coast of the Buenos Aires Province, *J. Coastal Res.*, 23, 119-126, 2007.
- Di Paola, G.: Geological and geo-morphological characterization of coastal Sele Plain (Campania, Italy) and considerations about its vulnerability, PhD Thesis, Università degli Studi del Molise, Italy, 2011.

1 Du, Y., Vachon, P. W., and Wolfe, J.: Wind Direction Estimation from SAR images of the Ocean
2 using Wavelet Analysis, *Can. J. Remote Sens.*, 28, 498-509, 2002.

3 Gornitz, M. V., Daniels, R. C., White, T. W., and Birdwell, K. R.: The development of a coastal
4 risk assessment database: vulnerability to sea-level rise in the U.S. southeast, *J. Coastal Res.*,
5 *Special Issue 12*, 327-338, 1994.

6 Gornitz, V. M., Beaty, T. W., and Daniels, R. C.: A coastal hazards data base for the U.S. West
7 Coast, Carbon Dioxide Information Analysis Center, Oak Ridge National Laboratory, Oak ridge,
8 Tennessee, 162, 1997.

9 Harlan, J. A. Jr.: Short Time Scale Effects on High Frequency Radar-Derived Current Velocity
10 Measurements, University of Colorado at Boulder, Ph.D. Dissertation, 2005.

11 Hasselmann, K., Barnett, T. P., Bouws, E., Carlson, H., Cartwright, D. E., Enke, K., Ewing, J. A.,
12 Gienapp, H., Hasselmann, D. E., Kruseman, P., Meerburg, A., Müller, P., Olbers, D. J., Richter,
13 K., Sell, W., and Walden, H.: Measurements of wind-wave growth and swell decay during the
14 Joint North Sea Wave Project (JONSWAP), *Dtsch. Hydrogr. Z. Suppl.*, 12, 1–95, 1973.

15 Holthuijsen, L. H., Booij, N., and Ris, R. C.: A spectral wave model for the coastal zone, in:
16 *Proceedings of the 2nd International Symposium on Ocean Wave Measurement and Analysis*,
17 New Orleans, 630-641, 1993.

18 Holthuijsen, L., Booij, N., Bertotti, L.: The propagation of wind errors through ocean wave
19 hindcasts. *J. Offshore Mech. Arct. Eng.* 118, 184-189, 1996.

20 Horstmann, J., Koch, W. and Lehner, S.: Wind Fields Retrieved from SAR in Comparison to
21 Numerical Models, in *Proceedings of Sixth International Winds Workshop*, Madison, Wisconsin,
22 USA, 7-10 May, 2002, EUM P 35, ISBN 92-9110-048-1, ISSN 1023-0416, 2002.

23 Italian Space Agency (ASI) – COSMO-SkyMed Mission: COSMO-SkyMed System Description
24 & User Guide, Online, Available at: <http://www.asi.it/it/flash/osservare/cosmoskymed/>, 2012.

25 Janssen, P.: *The Interaction of Ocean Waves and Wind*, Cambridge University Press, UK, 2004.

26 Johannessen, O. M., Sandven, S., Jenkins, A. D., Durand, D., Pettersson, L. H., Espedal, H.,
27 Evensen, G., and Hamre, T.: Satellite earth observation in operational oceanography. *Coast. Eng.*,
28 41, 155-176, 2000.

1 Kerbaol, V., Chapron, B., and Vachon, P.W.: Analysis of ERS-1/2 Synthetic Aperture Radar
2 wave mode imageries, *J. Geophys. Res.*, 103, 7833-7846, 1998.

3 Korsbakken, E., Johannessen, J. A., and Johannessen, O. M.: Coastal Wind Field Retrievals from
4 ERS Synthetic Aperture Radar Image, *J. Geophys. Res.*, 103, 7857-7874, 1998.

5 Kriebel, D. L., and Dean, R.G.: Convolution method for time-dependent beach-profile response, *J.*
6 *WATERW PORT C-ASCE*, 119, 204-207, 1993.

7 Lee, P. H. Y., Barter, J. D., Beach, K. L., Hindman, C. L., Lake, B. M., Rungaldier, H., Shelton, J.
8 C., Williams, A. B., Yee, R., and Yuen, H. C.: X band microwave backscattering from ocean
9 waves, *J. Geophys. Res.*, 100, 2591-2611, 1995.

10 Mallat, S. G.: A Theory for Multiresolution Signal Decomposition: the Wavelet Representation,
11 *IEEE T. Pattern Anal.*, 11, 674-693, 1989.

12 Migliaccio, M., Montuori, A., and Nunziata, F.: X-band Azimuth cut-off for wind speed retrieval
13 by means of COSMO-SkyMed SAR data, in: *Proceedings of IEEE/OES Baltic International*
14 *Symposium, Klaipeda, Lithuania, 8-10 May 2012, 1-4, 2012.*

15 Monaldo, F. M., Thompson, D. R., Winstead, N. S., Pichel, W. G., Clemente-Colon, P., and
16 Christiansen, M. B.: Ocean wind field mapping from synthetic aperture radar and its application
17 to research and applied problems. *Johns Hopkins Apl. Tech. Dig.*, 26, 102-113, 2005.

18 Montuori, A., Migliaccio, M., and Nunziata, F.: Wind Speed Estimation in the Tyrrhenian Sea by
19 Means of X-band COSMO-SkyMed SAR Data, in: *Proceedings of Tyrrhenian Workshop on*
20 *Advances in Radar and Remote Sensing 2012, Naples, Italy, 12-14 September 2012.*

21 Nicholls, R. J. and de la Vega-Leinert: Synthesis and up-scaling of sea-level rise vulnerability
22 assessment studies (SURVAS): SURVAS methodology, *Flood Hazard Research Centre –*
23 *Middlesex University, 2000.*

24 Schiavulli, D., Sorrentino, A., and Migliaccio, M.: An Automatic Procedure for Scalping
25 suppression and Homogeneity Analysis of Sea X-Band CSK SAR Images, *Atti della Fondazione*
26 *Giorgio Ronchi - Anno LXVII, 66, 27-38, 2011.*

27 Schiavulli, D., Sorrentino, A., and Migliaccio, M.: An Innovative Technique for Postprocessing
28 Descalping, *IEEE Geosci. Remote S.*, PP, 1-4, 2012.

- 1 Schulz-Stellenfleth, J. and Lehner, S.: Measurement of 2-D sea surface elevation fields using
2 complex synthetic aperture radar data, *IEEE T. Geosci. Remote*, 42, 1149-1160, 2004.
- 3 Stockdon, H. F., Holman, R. A., Howd, P. A., Sallenger, A. H.: Empirical parameterization of
4 setup, swash, and run-up, *Coast. Eng.*, 53, 573-588, 2006.
- 5 Portabella, M.: Wind Field Retrieval from Satellite Radar Systems. PhD Thesis, University of
6 Barcelona, ISBN: 90-6464-499-3, 2002.
- 7 Teixeira, J., Abreu, M., Soares, C.: Uncertainty of ocean wave hindcasts due to wind modelling. *J.*
8 *Offshore Mech. Arct. Eng.* 117, 294-297, 1995.
- 9 Tolman, H. L.: A third-generation model for wind waves on slowly varying, unsteady and
10 inhomogeneous depths and currents, *J. Phys. Oceanogr.*, 21, 782–797, 1991.
- 11 Tolman, H. L.: User manual and system documentation of WAVEWATCH-III version 1.15,
12 Technical Note 151, NOAA/NWS/NCEP/OMB, Washington DC, United States, 97 pp., 1997.
- 13 Tolman, H. L.: User manual and system documentation of WAVEWATCH-III version 1.18,
14 Technical Note 166, NOAA/NWS/NCEP/OMB, Washington DC, United States, 110 pp., 1999.
- 15 Tolman, H. L.: User manual and system documentation of WAVEWATCH III version 3.14,
16 Technical Note 276, NOAA/NWS/NCEP/MMAB, Washington DC, United States, 194 pp., 2009.
- 17 WAMDI Group: The WAM model - A third generation ocean wave prediction model, *J. Phys.*
18 *Oceanogr.*, 18, 1775–1810, 1988.
- 19 Whitham, G. B.: *Linear and Nonlinear Waves*, John Wiley, New York, 636 pp., 1974.

1 Table 1: Classification of I_R , I_{Ru} , E and I_i index values.

Class	Stability	Low	Moderate	High
Value	1	2	3	4
I_R	$R_{max}/L \% < 15$	$15 \leq R_{max}/L \% < 30$	$30 \leq R_{max}/L \% < 50$	$R_{max}/L \% \geq 50$
I_{Ru}	$X_{max}/L \% < 40$	$40 \leq X_{max}/L \% < 60$	$60 \leq X_{max}/L \% < 80$	$X_{max}/L \% \geq 80$
E	$V_E(\text{m/yr}) < 0.5$	$0.5 \leq V_E(\text{m/yr}) < 1.0$	$1.0 \leq V_E(\text{m/yr}) < 2.0$	$V_E(\text{m/yr}) \geq 2.0$
I_i	3.0	4.0 - 6.0	7.0 - 9.0	10.0 - 12.0

1 Table 2. Wave storms of winter season 2010, used for both SWAN simulation and CVA purposes.

	Reference Buoy				ECMWF		SAR		ECMWF-SAR	
Wave Storm	H_s (m)	T_p (s)	D_w (°N)	T_D (h)	H_s (m)	T_D (h)	H_s (m)	T_D (h)	H_s (m)	T_D (h)
November 8-10 th 2010	4.23	9.5	218	55	5.5	55	2.4	55	3.65	55
December 17-18 th 2010	5.01	9.5	231	24	5.0	24	2.5	15	3.4	15
December 23-25 th 2010	4.29	10	255	48	4.0	53	2.4	48	3.4	48

1 Table 3. Beach width classification of the different stretches along the Sele coastal plain.

L (m) (2010)	Mouth of Picentino (P1-P2)		Mouth of Tuscano (P3-P4)		Mouth of Sele (P5-P6-P7)		Mouth of Solofrone (P8-P9-P10)	
	Extension (m)	(%)	Extension (m)	(%)	Extension (m)	(%)	Extension (m)	(%)
Wide (L>50)	-	-	800	32	-	-	1,200	60
Medium (20<L<50)	1,200	48	1,700	68	2,050	82	800	40
Restricted (L<20)	1,300	52	-	-	350	14	-	-
Defense works			-	-	100	4	-	-

1 Table 4. Morpho-sedimentary features and CVA parameters for each profile of Sele coastal plain.

	P1	P2	P3	P4	P5	P6	P7	P8	P9	P10
μ_s (mm)	5.037	0.971	0.753	0.687	4.487	0.444	0.493	0.341	0.396	0.346
L (m)	20.4	27.3	20.4	26.2	26.3	25.5	15.8	41.6	57.7	47.1
β (%)	11.2	10.1	9.6	13.7	5.7	14.7	11.9	6.8	5.9	15.0
V_E (m/y)	0.71		1.20		2.17			0.08		
E	2 (Low)		3 (Moderate)		4 (High)			1 (Stable)		

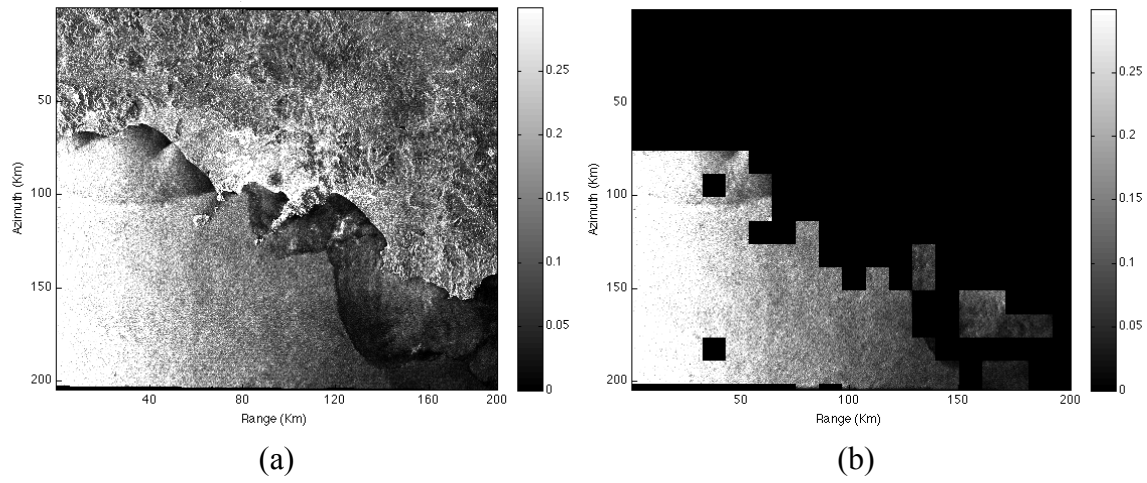


Figure 1. X-band Level 1B DGM ScanSAR Huge Region COSMO-SkyMed© SAR data acquired on 17 December 2010 at 18:00 UTC. (a) VV-polarized NRCS. (b) Output of the pre-processing step relevant to the SAR wind field retrieval approach.

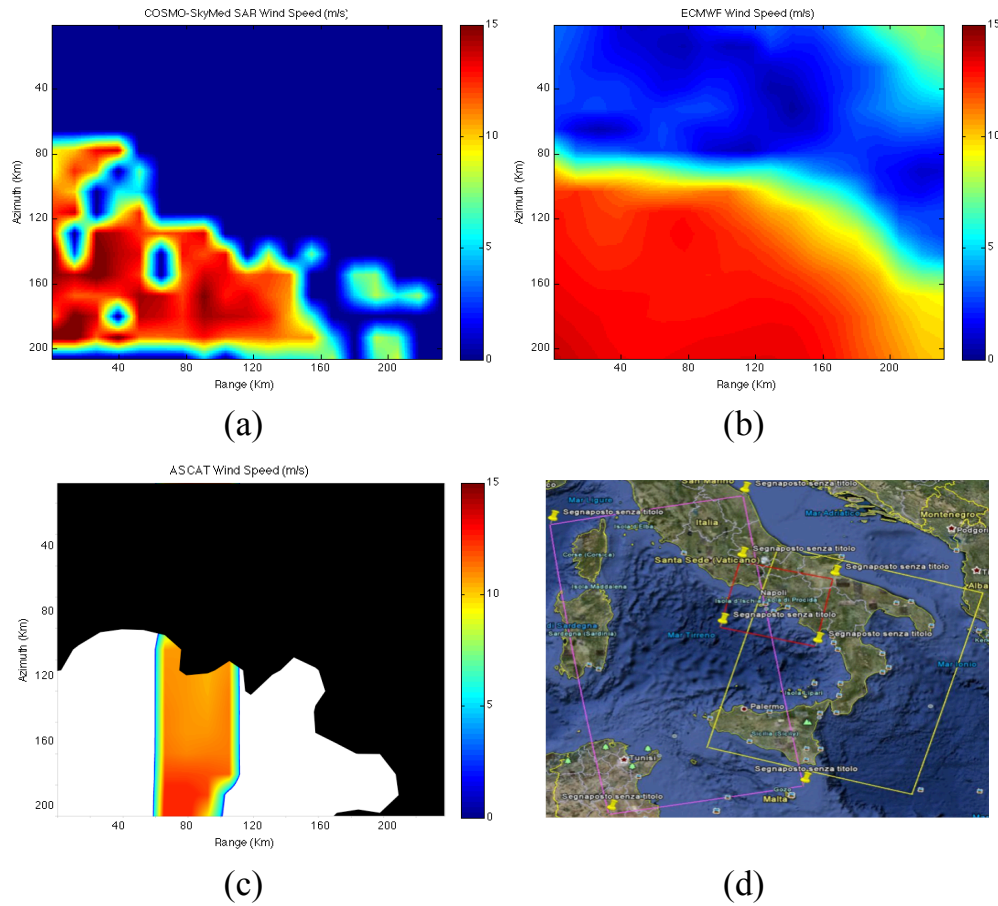


Figure 2. Experimental results relevant to the SAR-based wind speed estimation for the X-band Level 1B DGM ScanSAR Huge Region COSMO-SkyMed© SAR data acquired on 17 December 2010 at 18:00 UTC. (a) X-band SAR-derived wind speed estimation over a sub-image scale of 12.5km×12.5km. (b) Timely and spatially co-located ECMWF model wind speed. (c) Timely and spatially co-located ASCAT scatterometer wind speed. (d) Footprints of the ASCAT scatterometer wind speeds acquired before (purple box) and after (yellow box) the SAR acquisition, whose footprint is shown red color.

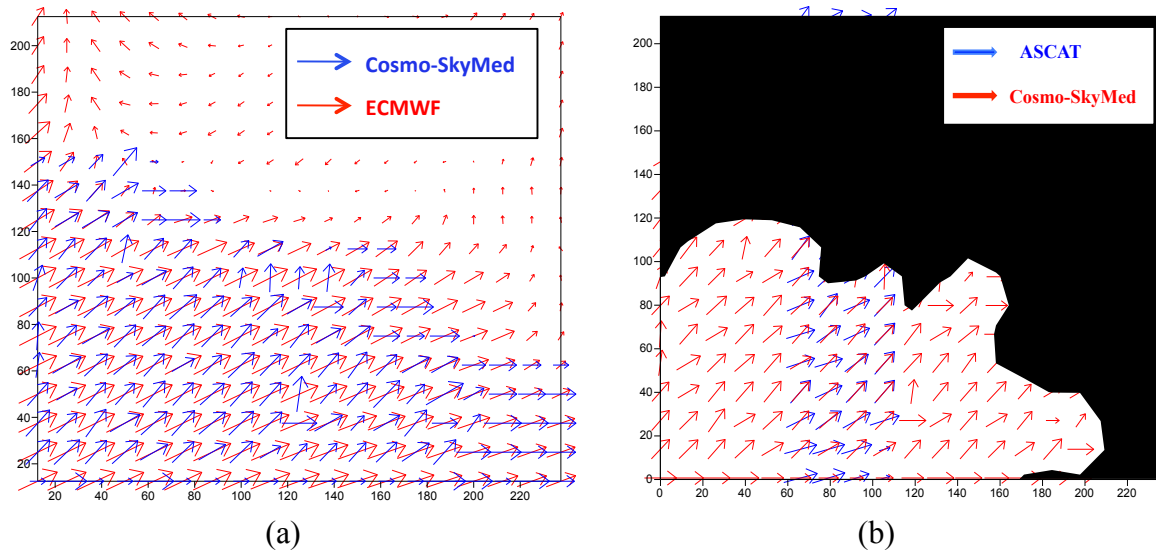


Figure 3. Experimental results relevant to the SAR-based wind direction estimation for the X-band Level 1B DGM ScanSAR Huge Region COSMO-SkyMed© SAR data acquired on 17 December 2010 at 18:00 UTC. (a) Comparison between X-band SAR-derived wind direction estimation and the reference ECMWF model wind direction over a sub-image scale of 12.5km×12.5km. (b) Comparison between X-band SAR-derived wind direction estimation and the reference ASCAT scatterometer wind direction over a sub-image scale of 12.5km×12.5km.

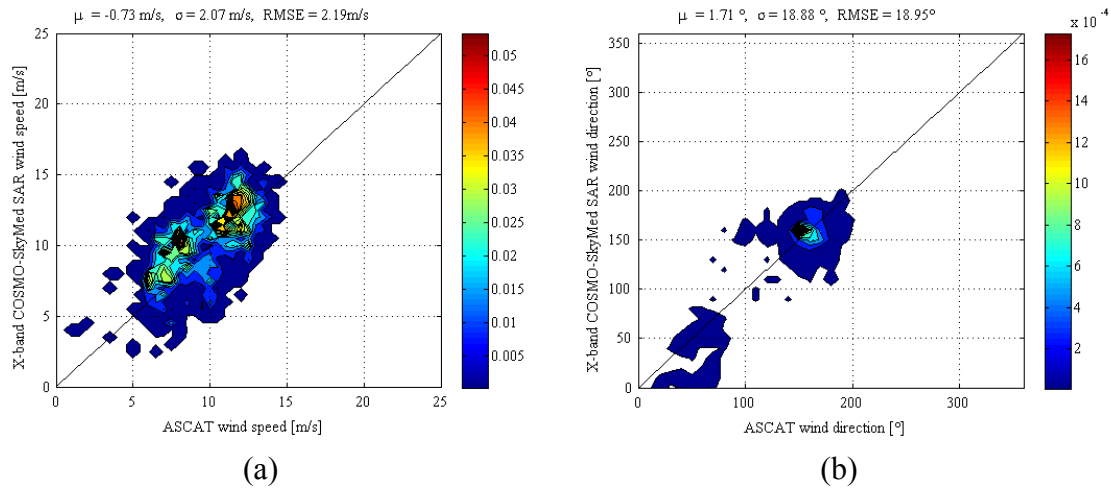
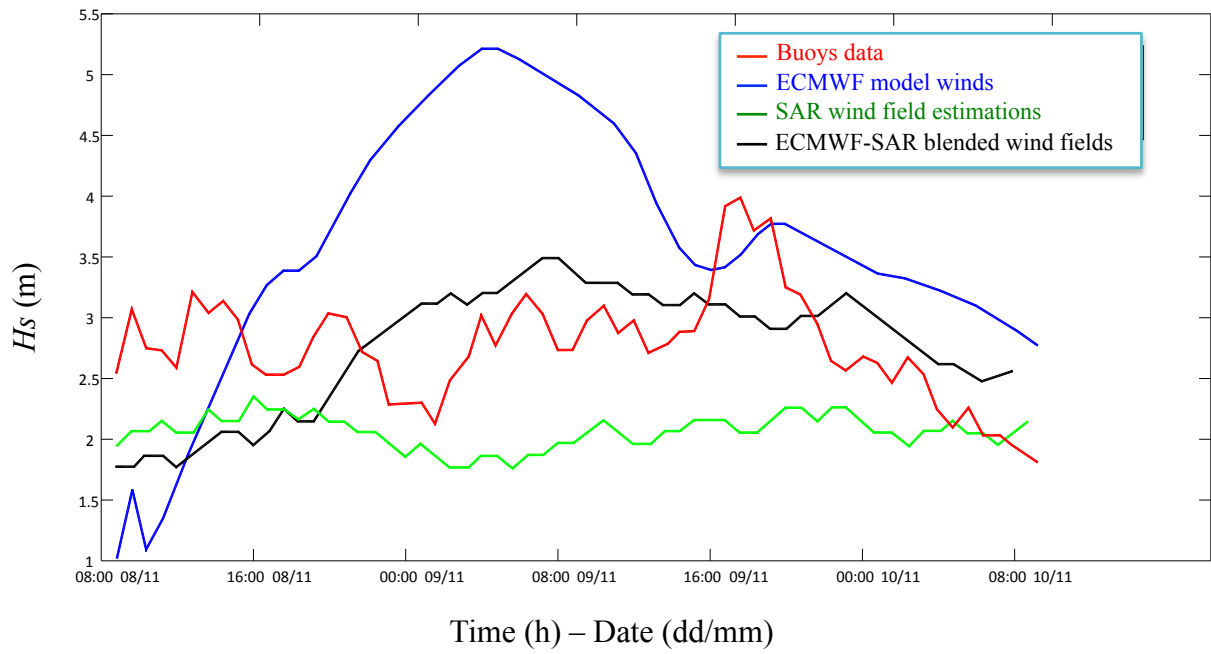


Figure 4. 2-D probability density scatter plot relevant to the comparison between the 12.5km×12.5km X-band COSMO-SkyMed© SAR-derived wind field estimation and the 12.5km×12.5km ASCAT scatterometer reference ground truth, for the whole processed COSMO-SkyMed© SAR data set. (a) Wind speed inter-comparison scatter plot. (b) Wind direction inter-comparison scatter plot.



1

2

3 **Figure 5.** Simulated and measured significant wave height H_s for the winter storm of 8-10
4 November 2010. Comparison among buoys data (red line), ECMWF (blue line), SAR (green
5 line), and ECMWF-SAR blended wind fields (black line).

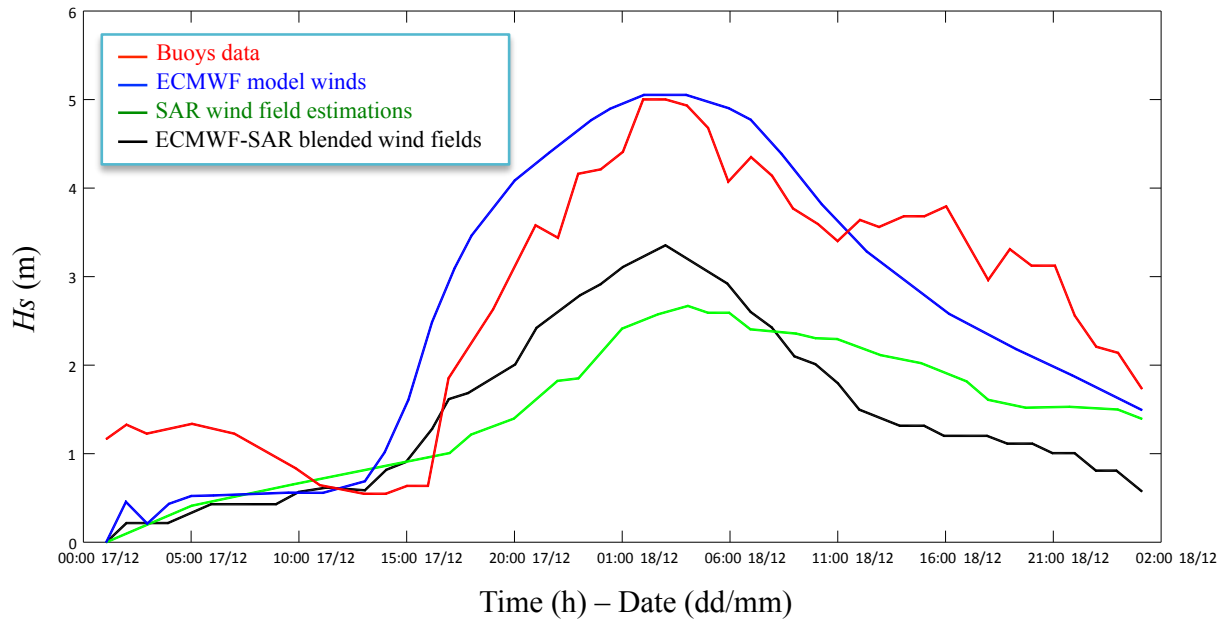
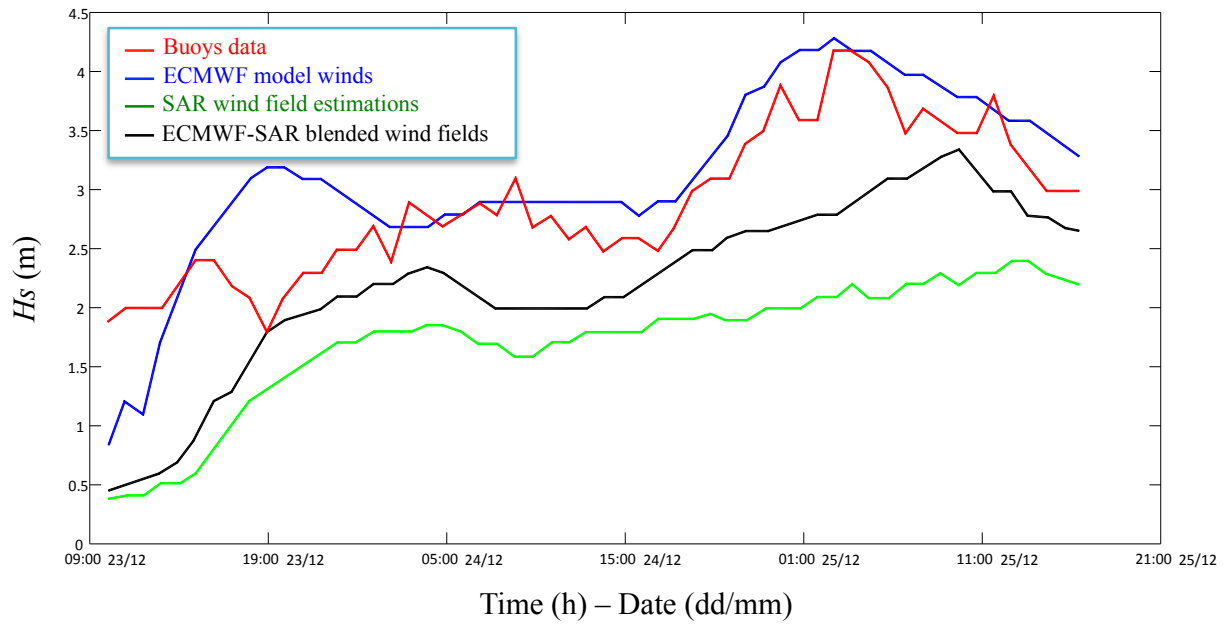


Figure 6. Simulated and measured significant wave height H_s for the winter storm of 17-18 December 2010. Comparison among buoys data (red line), ECMWF (blue line), SAR (green line) and ECMWF-SAR blended wind fields (black line).



1

2

3 **Figure 7.** Simulated and measured significant wave height H_s for the winter storm of 23-25
 4 December 2010. Comparison among buoys data (red line), ECMWF (blue line), SAR (green line)
 5 and ECMWF-SAR blended wind fields (black line).

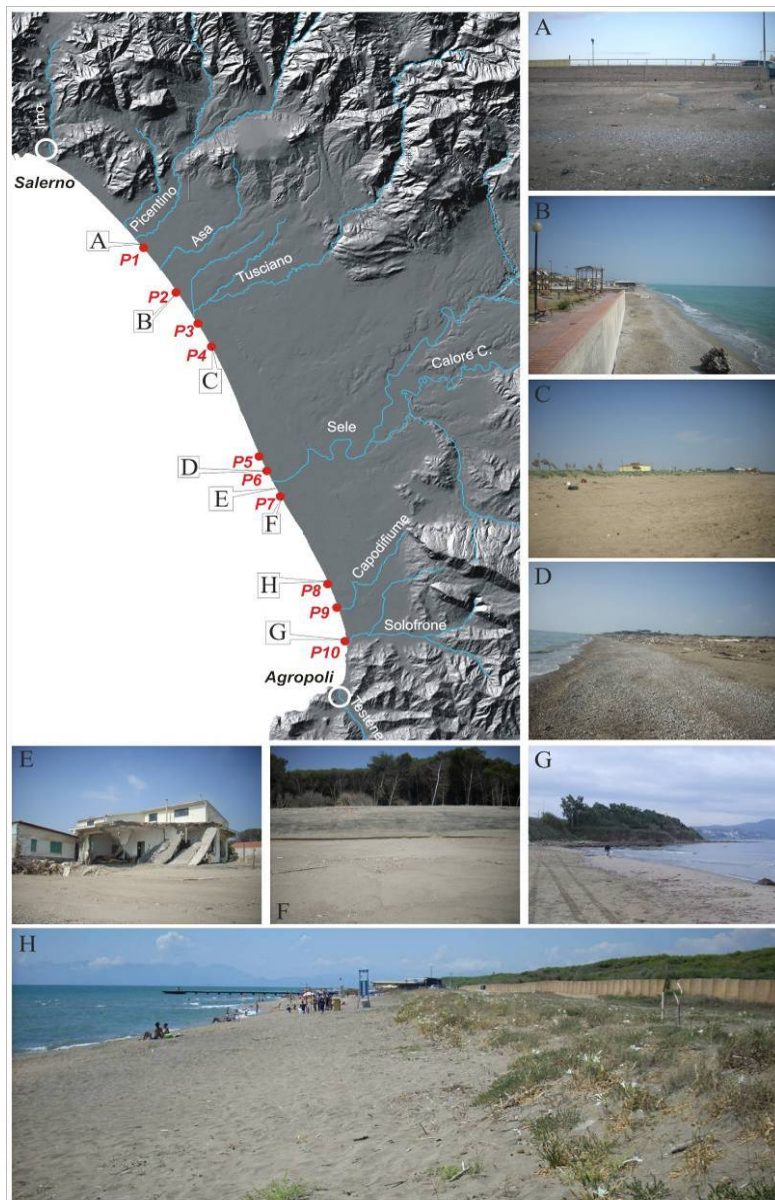


Figure 8. Detail of the coast Sele Plain: A) profile P1 without dune; B) the littoral zone, near the P2 profile; C) dune on profile P4 with the presence of pioneer vegetation; D) emerged and tidal beach on P6 profile; E) house belonging to the village Merola, located at the left bank of the Sele mouth; F) Profile P7, with carved dune; G) the end of physiographic unit near profile P10; H) dune and emerged beach of profile P8 with the presence of pioneer vegetation on the dune. All the beach profiles are detailed in Fig. 9.

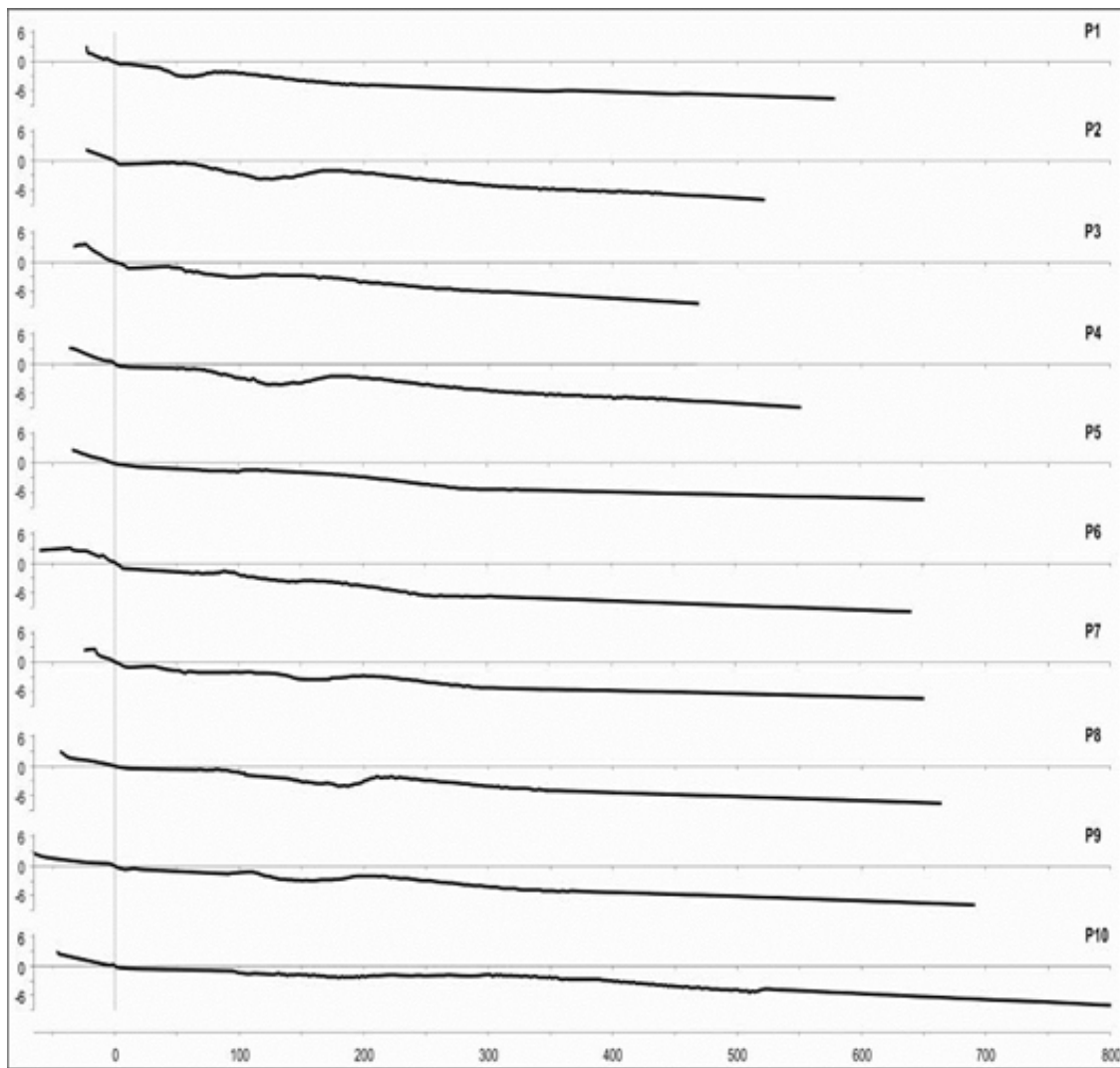


Figure 9. Topographical beach profiles carried out in the Sele coastal plain.

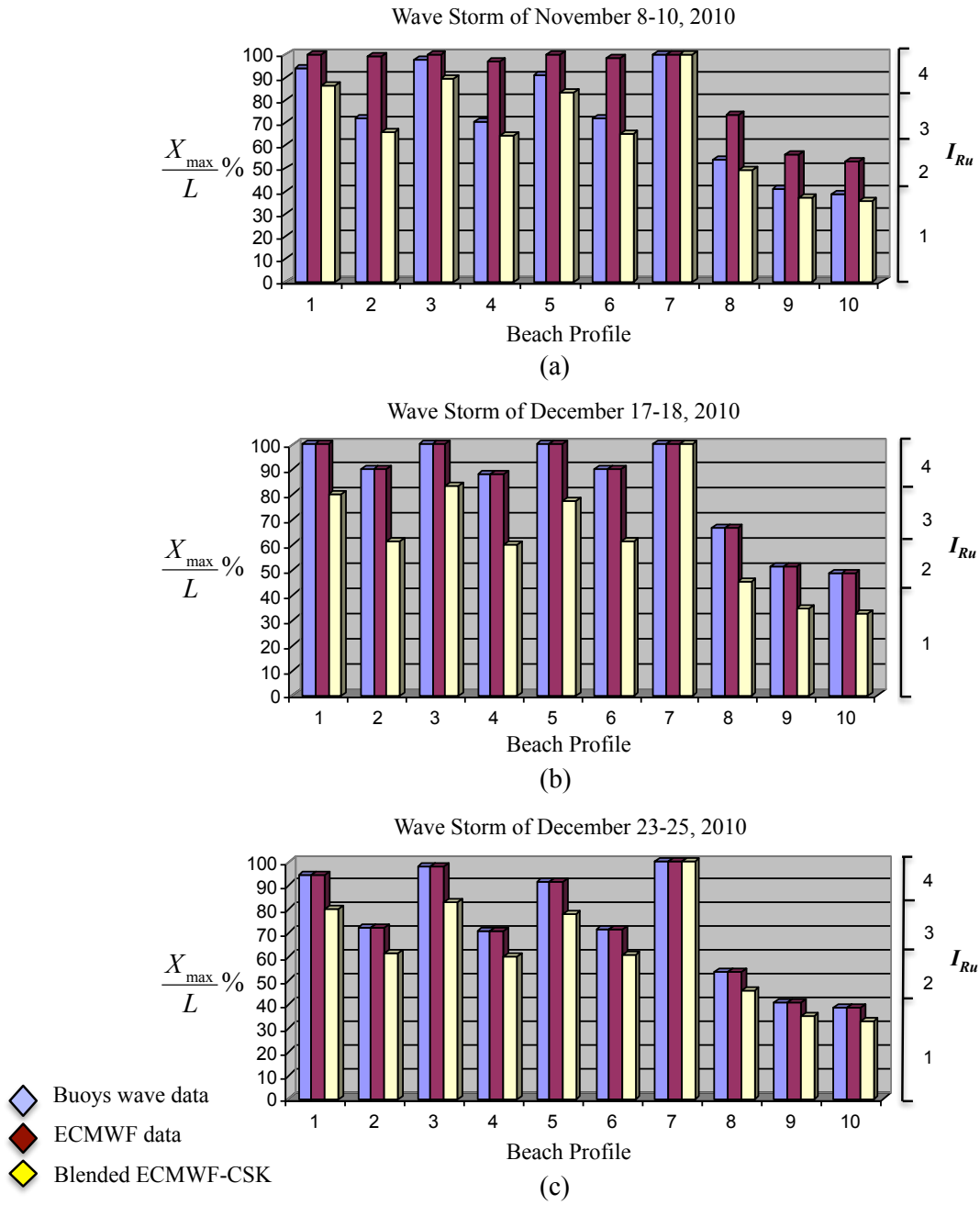


Figure 10. X_{max}/L % and I_{Ru} values, obtained through the buoys data (purple bars), ECMWF model winds (red bars) and ECMWF-SAR blended wind field products (yellow bars), for the ten beach profiles of the considered test area. (a) Wave storm of 8-10 November 2010. (b) Wave storm of 17-18 December 2010. (c) Wave storm of 23-25 December 2010.

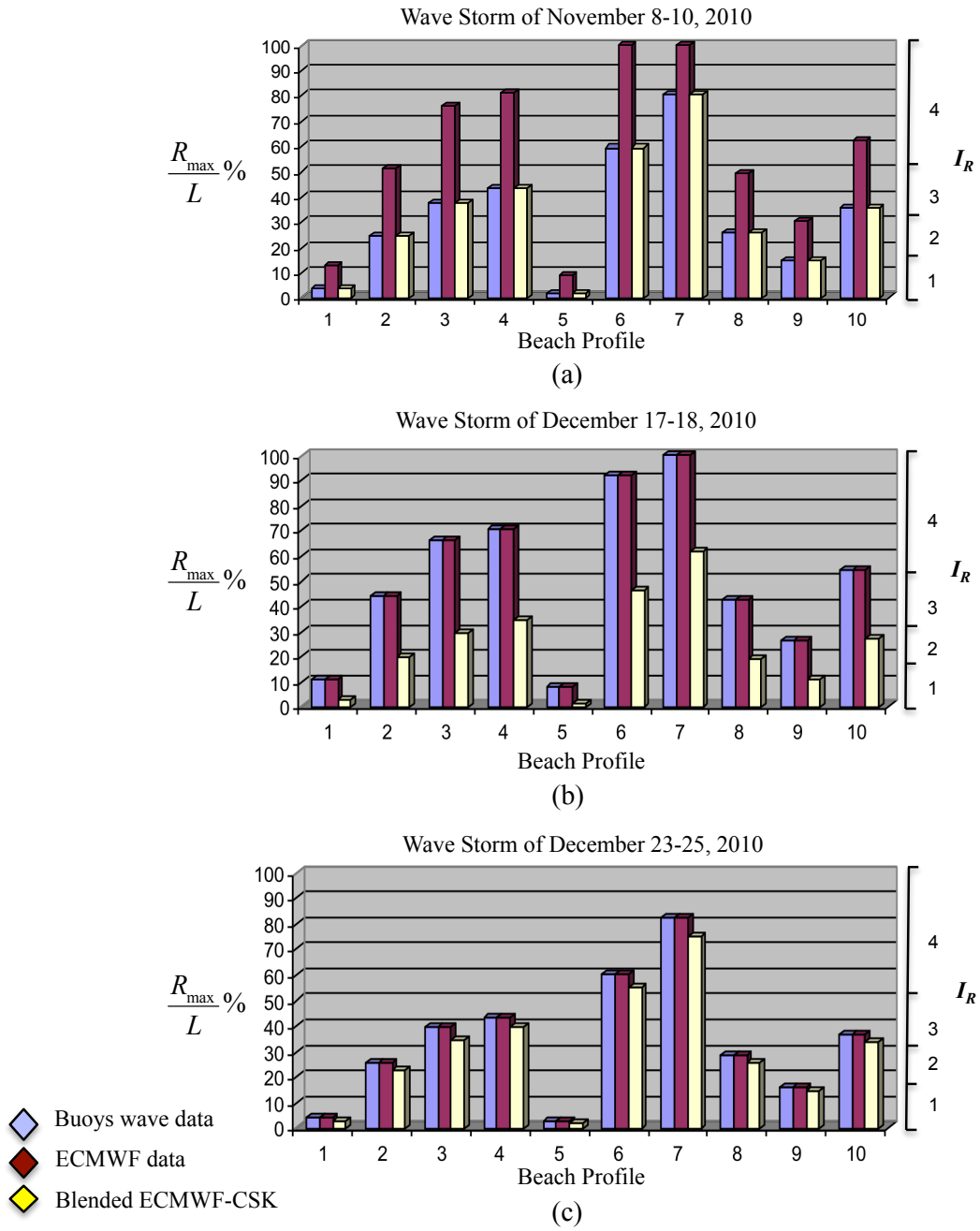


Figure 11. R_{max}/L % profile and I_R values, obtained through the buoys data (purple bars), ECMWF model winds (red bars) and ECMWF-SAR blended wind field products (yellow bars), for the ten beach profiles of the considered test area. (a) Wave storm of 8-10 November 2010. (b) Wave storm of 17-18 December 2010. (c) Wave storm of 23-25 December 2010.

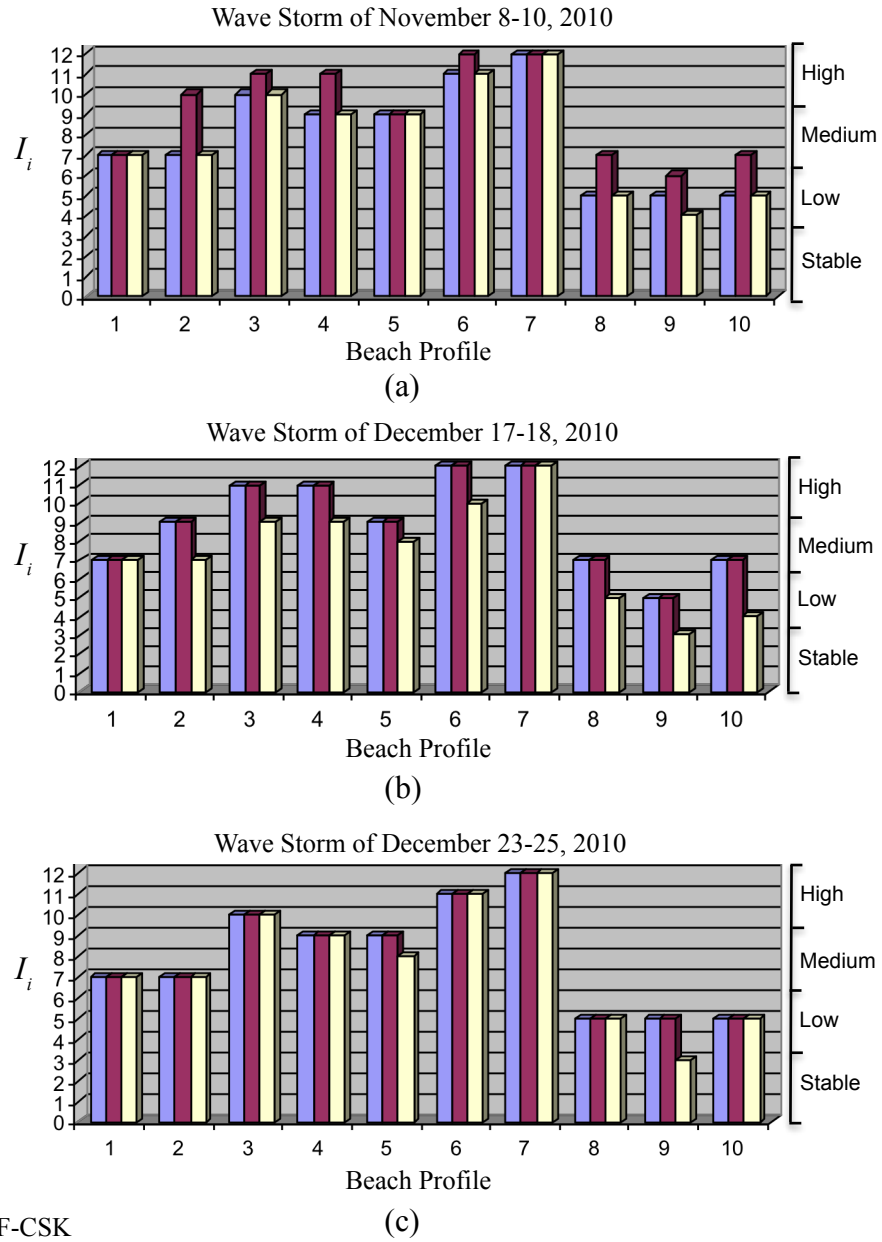


Figure 12. I_i values and vulnerability risk classification, obtained through buoys data (purple bars), ECMWF model winds (red bars) and ECMWF-SAR blended wind fields (yellow bars), for the ten beach profiles of the considered test area. (a) Wave storm of 8-10 November 2010. (b) Wave storm of 17-18 December 2010. (c) Wave storm of 23-25 December 2010.